downregulated in the cells transduced on day 9 as compared with nontransduced cells (**Figure 1b**). This might be because hepatic differentiation was selectively promoted and biliary differentiation was repressed by the transduction of HNF4α in hepatoblasts. The expression levels of the pancreas markers *PDX1*[23] and *NKX2.2*[24] did not make any change in the cells transduced on day 9 as compared with nontransduced cells (**Figure 1c**). Interestingly, the expression levels of the pancreas markers were upregulated, when Ad-HNF4α transduction was performed into DE cells (day 6) (**Figure 1c**). These results suggest that HNF4α might promote not only hepatic differentiation but also pancreatic differentiation, although the optimal stage of HNF4 transduction for the differentiation of each cell is different. We have confirmed that there was no difference between nontransduced cells and Ad-LacZ-transduced cells in the gene expression levels of all the markers investigated in **Figure 1a–c** (data not shown). We also confirmed that Ad vector-mediated gene expression in the human ESC-derived hepatoblasts (day 9) continued until day 14 and almost disappeared on day 18 (**Supplementary Figure S5**). These results indicated that the stage-specific HNF4α overexpression in human ESC-derived hepatoblasts (day 9) was essential for promoting efficient hepatic differentiation.

Transduction of HNF4α into human ESC- and iPSC-derived hepatoblasts efficiently promotes hepatic maturation

From the results of **Figure 1**, we decided to transduce hepatoblasts (day 9) with Ad-HNF4α. To determine whether hepatic maturation is promoted by Ad-HNF4α transduction, Ad-HNF4α-transduced cells were cultured until day 20 of differentiation according to the schematic protocol described in **Figure 2a**. After the hepatic maturation, the morphology of human ESCs was gradually changed into that of hepatocytes: polygonal with distinct round nuclei (day 20) (**Figure 2b**). Interestingly, a portion of the hepatocyte-like cells, which were ALB[20]-, CK18[21]-, CYP2D6-, and CYP3A4[25]-positive cells, had double nuclei, which was also observed in primary human hepatocytes (**Figure 2b,c**, and **Supplementary Figure S6**). We also examined the hepatic gene expression levels on day 20 of differentiation (**Figure 3a,b**). The gene expression analysis of *CYP1A2*, *CYP2C9*, *CYP2C19*, *CYP2D6*, *CYP3A4*, and *CYP7A1*[25] showed higher expression levels in all of Ad-SOX17-, Ad-HEX-, and Ad-HNF4α-transduced cells (three factors-transduced cells) as compared with those in both Ad-SOX17- and Ad-HEX-transduced cells (two factors-transduced cells) on day 20 (**Figure 3a**). The gene expression level of NADPH-CYP reductase

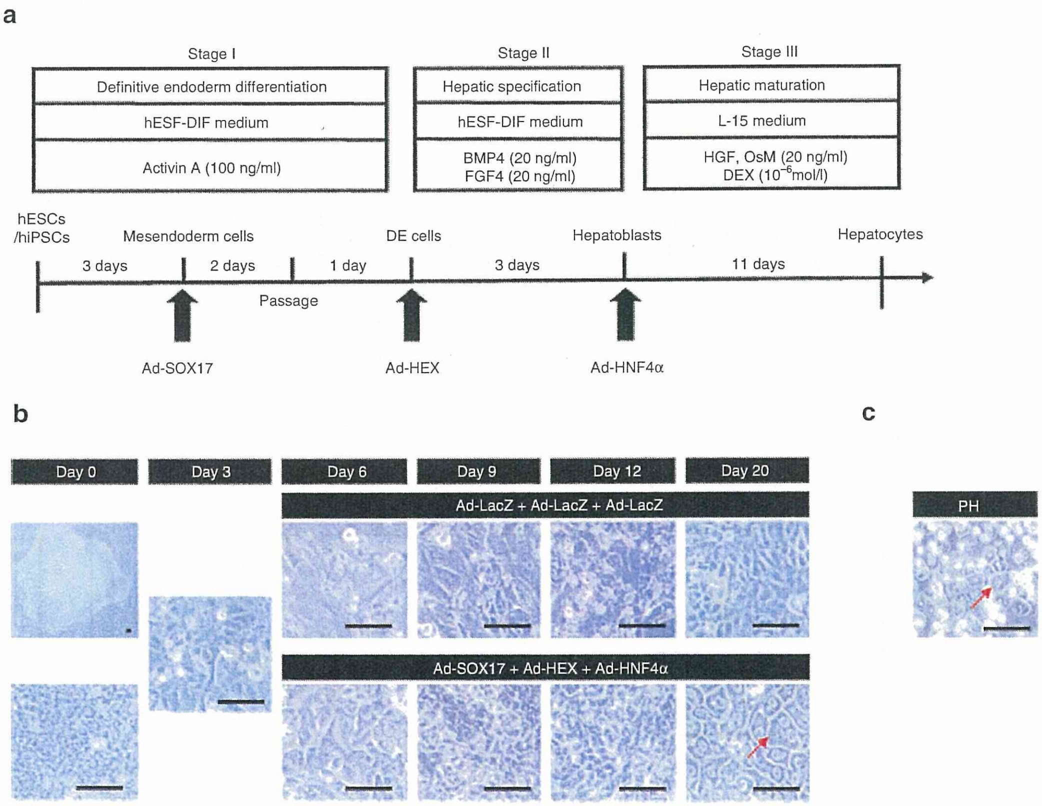

Figure 2 Hepatic differentiation of human ESCs and iPSCs transduced with three factors. (**a**) The procedure for differentiation of human ESCs and iPSCs into hepatocytes via DE cells and hepatoblasts is presented schematically. The hESF-DIF medium was supplemented with 10 µg/ml human recombinant insulin, 5 µg/ml human apotransferrin, 10 µmol/l 2-mercaptoethanol, 10 µmol/l ethanolamine, 10 µmol/l sodium selenite, and 0.5 mg/ml fatty-acid-free BSA. The L15 medium was supplemented with 8.3% tryptose phosphate broth, 8.3% FBS, 10 µmol/l hydrocortisone 21-hemisuccinate, 1 µmol/l insulin, and 25 mmol/l NaHCO$_3$. (**b**) Sequential morphological changes (day 0–20) of human ESCs (H9) differentiated into hepatocytes via DE cells and hepatoblasts are shown. Red arrow shows the cells that have double nuclei. (**c**) The morphology of primary human hepatocytes is shown. Bar represents 50 µm. BSA, bovine serum albumin; DE, definitive endoderm; ESC, embryonic stem cell; iPSC, induced pluripotent stem cell.

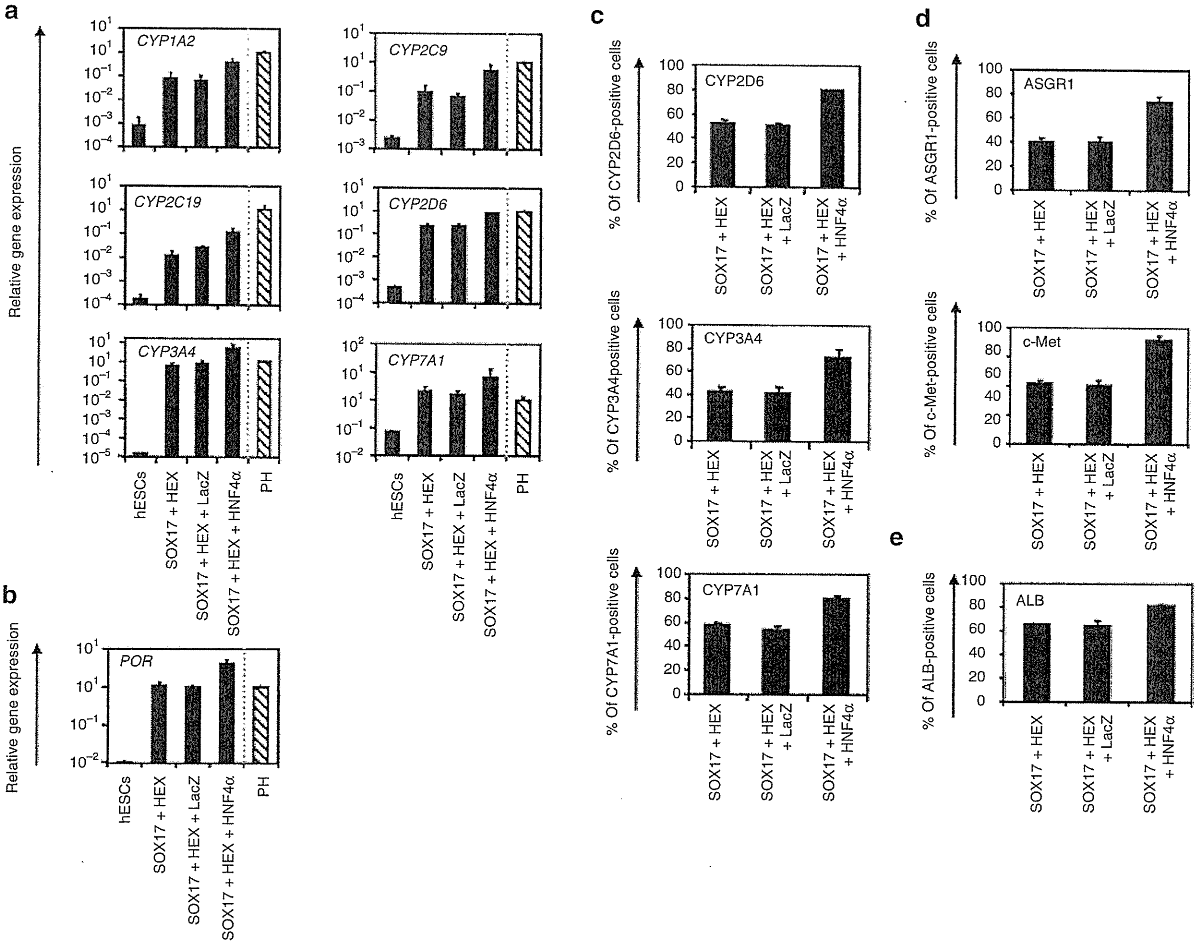

Figure 3 Transduction of HNF4α promotes hepatic maturation from human ESCs and iPSCs. (**a**,**b**) The human ESCs were differentiated into hepatocytes according to the protocol described in **Figure 2a**. On day 20 of differentiation, the gene expression levels of (**a**) CYP enzymes (*CYP1A2*, *CYP2C9*, *CYP2C19*, *CYP2D6*, *CYP3A4*, and *CYP7A1*) and (**b**) *POR* were examined by real-time RT-PCR in undifferentiated human ESCs (hESCs), the hepatocyte-like cells, and primary human hepatocytes (PH, hatched bar). On the y-axis, the expression level of primary human hepatocytes, which were cultured for 48 hours after the cells were plated, was taken as 1.0. (**c**–**e**) The hepatocyte-like cells (day 20) were subjected to immunostaining with (**c**) anti-drug-metabolizing enzymes (CYP2D6, CYP3A4, and CYP7A1), (**d**) anti-hepatic surface protein (ASGR1 and c-Met), and (**e**) anti-ALB antibodies, and then the percentage of antigen-positive cells was examined by flow cytometry on day 20 of differentiation. All data are represented as means ± SD ($n = 3$). ESC, embryonic stem cell; HNF4α, hepatocyte nuclear factor 4α; iPSC, induced pluripotent stem cell.

(POR)[26], which is required for the normal function of CYPs, was also higher in the three factors-transduced cells (Figure 3b). The gene expression analysis of ALB, α-1-antitrypsin (α-1-AT), transthyretin, hepatic conjugating enzymes, hepatic transporters, and hepatic transcription factors also showed higher expression levels in the three factors-transduced cells (**Supplementary Figures S7** and **S8**). Moreover, the gene expression levels of these hepatic markers of three factor-transduced cells were similar to those of primary human hepatocytes, although the levels depended on the type of gene (Figure 3a,b, and **Supplementary Figures S7** and **S8**). To confirm that similar results could be obtained with human iPSCs, we used three human iPS cell lines (201B7, Dotcom, and Tic). The gene expression of hepatic markers in human ESC- and iPSC-derived hepatocytes were analyzed by real-time reverse transcription-PCR on day 20 of differentiation. Three human iPS cell lines as well as human ESCs also effectively differentiated into hepatocytes in response to transduction of the three factors (**Supplementary Figure S9**). Interestingly, we observed differences in the hepatic maturation efficiency among the three human iPS cell lines. That is, two of the human iPS cell lines (Tic and Dotcom) were more committed to the hepatic lineage than another human iPS cell line (201B7). Because almost homogeneous hepatocyte-like cells would be more useful in basic research, regenerative medicine, and drug discovery, we also examined whether our novel methods for hepatic maturation could generate a homogeneous hepatocyte population by flow cytometry analysis (Figure 3c–e). The percentages of CYP2D6-, CYP3A4-, and CYP7A1-positive cells were ~80% in the three factors-transduced cells, while they were ~50% in the two factors-transduced cells (Figure 3c). The percentages of hepatic surface antigen (asialoglycoprotein receptor 1 [ASGR1] and met proto-oncogene (c-Met))-positive cells (Figure 3d) and ALB-positive cells (Figure 3e) were also ~80% in the three factors-transduced cells. These results indicated that a nearly homogeneous population was obtained by our differentiation protocol using the transduction of three functional genes (SOX17, HEX, and HNF4α).

The three factors-transduced cells have characteristics of functional hepatocytes

The hepatic functions of the hepatocyte-like cells, such as the uptake of low-density lipoprotein (LDL) and CYP enzymes activity, of the hepatocyte-like cells were examined on day 20 of differentiation. Approximately 87% of the three factors-transduced cells uptook LDL in the medium, whereas only 44% of the two factors-transduced cells did so (**Figure 4a**). The activities of CYP enzymes of the hepatocyte-like cells were measured according to the metabolism of the CYP3A4, CYP2C9, or CYP1A2 substrates (**Figure 4b**). The metabolites were detected in the three factors-transduced cells and their activities were higher than those of the two factors-transduced cells (dimethyl sulfoxide (DMSO) column). We further tested the induction of CYP3A4, CYP2C9, and CYP1A2 by chemical stimulation, since CYP3A4, CYP2C9, and CYP1A2 are the important prevalent CYP isozymes in the liver and are involved in the metabolism of a significant proportion of the currently available commercial drugs (rifampicin or omeprazole column). It is well known that CYP3A4 and CYP2C9 can be induced by rifampicin, whereas CYP1A2 can be induced by omeprazole. The hepatocyte-like cells were treated with either of these. Although undifferentiated human ESCs responsed to neither rifampicin nor omeprazole (data not shown), the hepatocyte-like cells produced more metabolites in response to chemical stimulation as well as primary hepatocytes (**Figure 4b**). The activity levels of the hepatocyte-like cells as compared with those of primary human hepatocytes depended on the types of CYP; the CYP3A4 activity of the hepatocyte-like cells was similar to that of primary human hepatocytes, whereas the CYP2C9 and CYP1A2 activities of the hepatocyte-like cells were slightly lower than those of primary human hepatocytes (**Figure 3a**). These results indicated that high levels of functional CYP enzymes were detectable in the hepatocyte-like cells.

The metabolism of diverse compounds involving uptake, conjugation, and the subsequent release of the compounds is an important function of hepatocytes. Uptake and release of Indocyanine green (ICG) can often be used to identify hepatocytes in ESC differentiation models.[27] To investigate this function in our hepatocyte-like cells, we compared this ability of the three factors-transduced cells with that of the two factors-transduced cells on day 20 of differentiation (**Figure 4c**). The three factors-transduced cells had more ability to uptake ICG and to excrete ICG by culturing without ICG for 6 hours. We also examined whether the hepatocyte-like cells could store glycogen, a characteristic of functional hepatocytes (**Figure 4d**). On day 20 of differentiation, the three factors-transduced cells and the two factors-transduced cells were stained for cytoplasmic glycogen using the Periodic Acid-Schiff staining procedure. The three factors-transduced cells exhibited more abundant storage of glycogen than the two-factors-transduced cells. These results showed that abundant hepatic functions, such as uptake and excretion of ICG and storage of glycogen, were obtained by the transduction of three factors.

Many adverse drug reactions are caused by the CYP-dependent activation of drugs into reactive metabolites.[28] In order to examine metabolism-mediated toxicity and to improve the safety of drug candidates, primary human hepatocytes are widely used.[28] Because primary human hepatocytes have quite different characteristics among distinct lots and because it is difficult to purchase large amounts of primary human hepatocytes that have the same characteristics, hepatocyte-like cells are expected to be used for this purpose. To examine whether our hepatocyte-like cells could be used to predict metabolism-mediated toxicity, the hepatocyte-like cells were incubated with four substrates (troglitazone, acetaminophen, cyclophosphamide, and carbamazepine), which are known to generate toxic metabolites by CYP enzymes, and then the cell viability was measured (**Figure 4e**). The cell viability of the two factors plus Ad-LacZ-tansduced cells were higher than that of the three factors-transduced cells at each different concentration of four test compounds. These results indicated that the three factors-transduced cells could more efficiently metabolize the test compounds and thereby induce higher toxicity than either the two factors-transduced cells or undifferentiated human ESCs. The cell viability of the three factors-transduced cells was slightly higher than that of primary human hepatocytes.

HNF4α promotes hepatic maturation by activating mesenchymal-to-epithelial transition

HNF4α is known as a dominant regulator of the epithelial phenotype because its ectopic expression in fibroblasts (such as NIH 3T3 cells) induces mesenchymal-to-epithelial transition (MET)[11], although it is not known whether HNF4α can promote MET in hepatic differentiation. Therefore, we examined whether HNF4α transduction promotes hepatic maturation from hepatoblasts by activating MET. To clarify whether MET is activated by HNF4α transduction, the human ESC-derived hepatoblasts (day 9) were transduced with Ad-LacZ or Ad-HNF4α, and the resulting phenotype was analyzed on day 12 of differentiation (**Figure 5**). This time, we confirmed that HNF4α transduction decreased the population of N-cadherin (hepatoblast marker)-positive cells,[29] whereas it increased that of ALB (hepatocyte marker)-positive cells (**Figure 5a**). The number of CK7 (cholangiocyte marker)-positive population did not change (**Figure 5a**). To investigate whether these results were attributable to MET, the alteration of the expression of several mesenchymal and epithelial markers was examined (**Figure 5b**). The human ESC-derived hepatoblasts (day 9) were almost homogeneously N-cadherin[30] (mesenchymal marker)-positive and E-cadherin[11] (epithelial marker)-negative, demonstrating that human ESC-derived hepatoblasts have mesenchymal characteristics (**Figure 5a,b**). After HNF4α transduction, the number of E-cadherin-positive cells was increased and reached ~90% on day 20, whereas that of N-cadherin-positive cells was decreased and was less than 5% on day 20 (**Supplementary Figure S10**). These results indicated that MET was promoted by HNF4α transduction in hepatic differentiation from hepatoblasts. Interestingly, the number of growing cells was decreased by HNF4α transduction (**Figure 5c**), and the cell growth was delayed by HNF4α transduction (**Supplementary Figure S11**). This decrease in the number of growing cells might have been because the differentiation was promoted by HNF4α transduction. We also confirmed that MET was promoted by HNF4α transduction in the gene expression levels (**Figure 5d**).

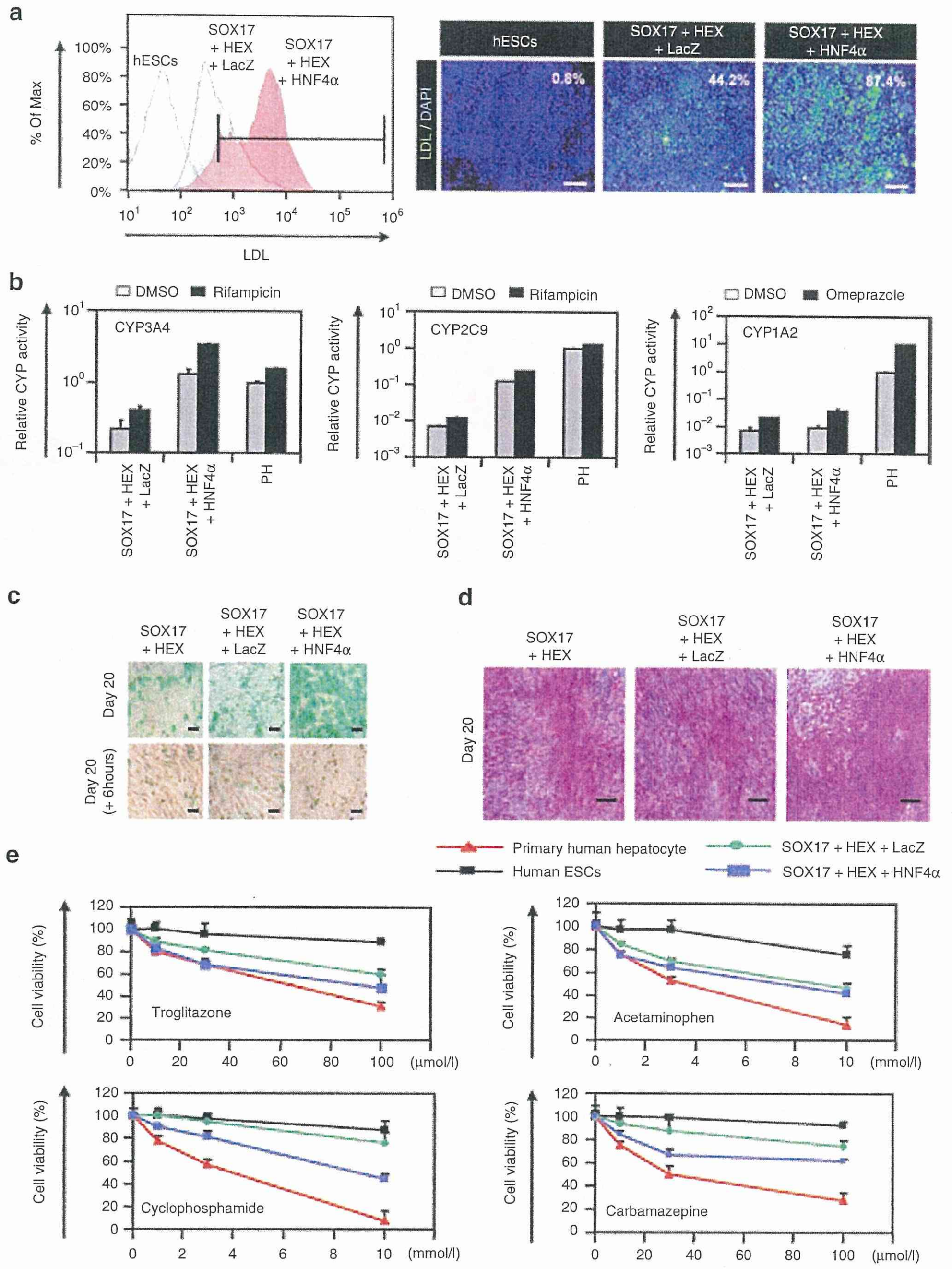

Figure 4 Transduction of the three factors enhances hepatic functions. The human ESCs were differentiated into hepatoblasts and transduced with 3,000 VP/cell of Ad-LacZ or Ad-HNF4α for 1.5 hours and cultured until day 20 of differentiation according to the protocol described in **Figure 2a**. The hepatic functions of the two factors plus Ad-LacZ-transduced cells (SOX17+HEX+LacZ) and the three factors-transduced cells (SOX17+HEX+HNF4α) were compared. (**a**) Undifferentiated human ESCs (hESCs) and the hepatocyte-like cells (day 20) were cultured with medium containing Alexa-Flour 488-labeled LDL (green) for 1 hour, and immunohistochemistry and flow cytometry analysis were performed. The percentage of LDL-positive cells was measured by flow cytometry. Nuclei were counterstained with DAPI (blue). The bar represents 100 μm. (**b**) Induction of CYP3A4 (left), CYP2C9 (middle), or CYP1A2 (right) by DMSO (gray bar), rifampicin (black bar), or omeprazole (black bar) in the hepatocyte-like cells (day 20) and primary human hepatocytes (PH), which were cultured for 48 hours after the cells were plated. On the y-axis, the activity of primary human hepatocytes that have been cultured with medium containing DMSO was taken as 1.0. (**c**) The hepatocyte-like cells (day 20) (upper column) were examined for their ability to take up Indocyanin Green (ICG) and release it 6 hours thereafter (lower column). (**d**) Glycogen storage of the hepatocyte-like cells (day 20) was assessed by Periodic Acid-Schiff (PAS) staining. PAS staining was performed on day 20 of differentiation. Glycogen storage is indicated by pink or dark red-purple cytoplasms. The bar represents 100 μm. (**e**) The cell viability of undifferentiated human ESCs (black), two factors plus Ad-LacZ-tansduced cells (green), the three factors-transduced cells (blue), and primary human hepatocytes (red) was assessed by Alamar Blue assay after 48 hours exposure to different concentrations of four test compounds (troglitazone, acetaminophen, cyclophosphamide, and carbamazepine). The cell viability is expressed as a percentage of cells treated with solvent only treat: 0.1% DMSO except for carbamazepine: 0.5% DMSO. All data are represented as means ± SD (*n* = 3). ESC, embryonic stem cell; DMSO, dimethyl sulfoxide; LDL, low-density lipoprotein.

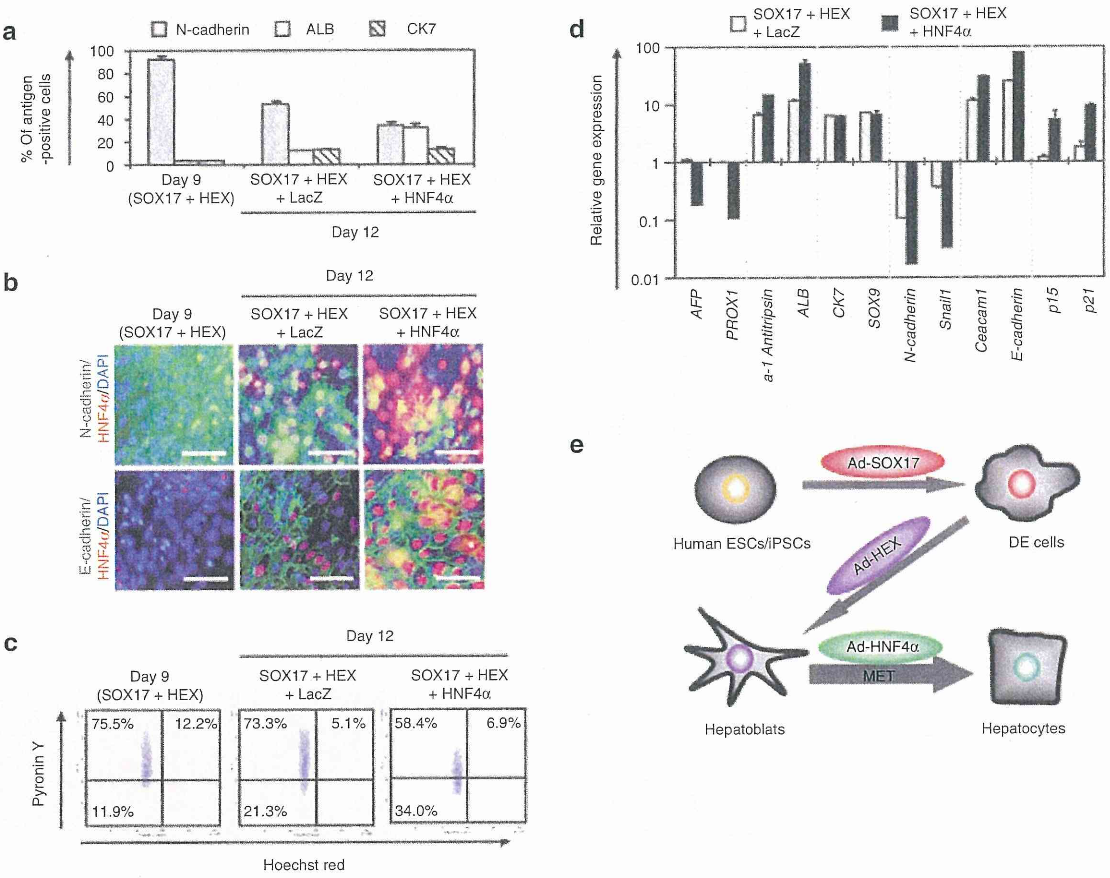

Figure 5 HNF4α promotes hepatic differentiation by activating MET. Human ESCs were differentiated into hepatoblasts according to the protocol described in **Figure 2a**, and then transduced with 3,000 VP/cell of Ad-LacZ or Ad-HNF4α for 1.5 hours, and finally cultured until day 12 of differentiation. (**a**) The hepatoblasts, two factors plus Ad-LacZ-transduced cells (SOX17+HEX+LacZ) (day 12), and the three factors-transduced cells (SOX17+HEX+HNF4α) (day 12) were subjected to immunostaining with anti-N-cadherin, ALB, or CK7 antibodies. The percentage of antigen-positive cells was measured by flow cytometry. (**b**) The cells were subjected to immunostaining with anti-N-cadherin (green), E-cadherin (green), or HNF4α (red) antibodies on day 9 or day 12 of differentiation. Nuclei were counterstained with DAPI (blue). The bar represents 50 μm. Similar results were obtained in two independent experiments. (**c**) The cell cycle was examined on day 9 or day 12 of differentiation. The cells were stained with Pyronin Y (y-axis) and Hoechst 33342 (x-axis) and then analyzed by flow cytometry. The growth fraction of cells is the population of actively dividing cells (G1/S/G2/M). (**d**) The expression levels of *AFP*, *PROX1*, *α-1-antitrypsin*, *ALB*, *CK7*, *SOX9*, *N-cadherin*, *Snail1*, *Ceacam1*, *E-cadherin*, *p15*, and *p21* were examined by real-time RT-PCR on day 9 or day 12 of differentiation. The expression level of hepatoblasts (day 9) was taken as 1.0. All data are represented as means ± SD ($n = 3$). (**e**) The model of efficient hepatic differentiation from human ESCs and iPSCs in this study is summarized. The human ESCs and iPSCs differentiate into hepatocytes via definitive endoderm and hepatoblasts. At each stage, the differentiation is promoted by stage-specific transduction of appropriate functional genes. In the last stage of hepatic differentiation, HNF4α transduction provokes hepatic maturation by activating MET. ESC, embryonic stem cell; HNF4α, hepatocyte nuclear factor 4α; iPSC, induced pluripotent stem cell; MET, mesenchymal-to-epithelial transition; RT-PCR, reverse transcription-PCR; VP, vector particle.

The gene expression levels of hepatocyte markers (*α-1-antitrypsin* and *ALB*)[20] and epithelial markers (*Ceacam1* and *E-cadherin*) were upregulated by HNF4α transduction. On the other hand, the gene expression levels of hepatoblast markers (*AFP* and *PROX1*)[31], mesenchymal markers (*N-cadherin* and *Snail*)[32], and cyclin dependent kinase inhibitor (*p15* and *p21*)[33] were downregulated by HNF4α transduction. HNF4α transduction did not change the expression levels of cholangiocyte markers (*CK7* and *SOX9*). We conclude that HNF4α promotes hepatic maturation by activating MET.

DISCUSSION

This study has two main purposes: the generation of functional hepatocytes from human ESCs and iPSCs for application to drug toxicity screening in the early phase of pharmaceutical development and; elucidation of the HNF4α function in hepatic maturation from human ESCs. We initially confirmed the importance of transcription factor HNF4α in hepatic differentiation from human ESCs by using a published data set of gene array analysis (**Supplementary Figure S1**).[34] We speculated that HNF4α transduction could enhance hepatic differentiation from human ESCs and iPSCs.

To generate functional hepatocytes from human ESCs and iPSCs and to elucidate the function of HNF4α in hepatic differentiation from human ESCs, we examined the stage-specific roles of HNF4α. We found that hepatoblast (day 9) stage-specific HNF4α transduction promoted hepatic differentiation (**Figure 1**). Because endogenous HNF4α is initially expressed in the hepatoblast,[9,10] our system might adequately reflect early embryogenesis. However, HNF4α transduction at an inappropriate stage (day 6 or day 12) promoted bidirectional differentiation; heterogeneous populations, which contain the hepatocytes and pancreas cells or hepatocytes and cholangiocytes, were obtained, respectively (Figure 1), consistent with a previous report that HNF4α plays an important role not only in the liver but also in the pancreas.[12] Therefore, we concluded that HNF4α plays a significant stage-specific role in the differentiation of human ESC- and iPSC-derived hepatoblasts to hepatocytes (Figure 5e).

We found that the expression levels of the hepatic functional genes were upregulated by HNF4α transduction (Figure 3a,b, and **Supplementary Figures S7** and **S8**). Although the c/EBPα and GATA4 expression levels of the three factors-transduced cells were higher than those of primary human hepatocytes, the FOXA1, FOXA2, FOXA3, and HNF1α, which are known to be important for hepatic direct reprogramming and hepatic differentiation,[35,36] expression levels of three factors-transduced cells were slightly lower than those of primary human hepatocytes (**Supplementary Figure S8**). Therefore, additional transduction of FOXA1, FOXA2, FOXA3, and HNF1α might promote further hepatic maturation. Some previous hepatic differentiation protocols that utilized growth factors without gene transfer led to the appearance only of heterogeneous hepatocyte populations.[4–6] The HNF4α transduction led not only to the upregulation of expression levels of several hepatic markers but also to an almost homogeneous hepatocyte population; the differentiation efficacy based on CYPs, ASGR1, or ALB expression was ~80% (Figure 3c–e). The efficient hepatic maturation in this study might be attributable to the activation of many hepatocyte-associated genes by the transduction of HNF4α, which binds to the promoters of nearly half of the genes expressed in the liver.[12] In the later stage of hepatic maturation, hepatocyte-associated genes would be strongly upregulated by endogenous transcription factors but not exogenous HNF4α because transgene expression by Ad vectors was almost disappeared on day 18 (**Supplementary Figure S5**). Another reason for the efficient hepatic maturation would be that sequential transduction of SOX17, HEX, and HNF4α could mimic hepatic differentiation in early embryogenesis.

Next, we examined whether or not the hepatocyte-like cells had hepatic functions. The activity of many kinds of CYPs was upregulated by HNF4α transduction (Figure 4b). Ad-HNF4α-transduced cells exhibit many characteristics of hepatocytes: uptake of LDL, uptake and excretion of ICG, and storage of glycogen (Figure 4a,c,d). Many conventional tests of hepatic characteristics have shown that the hepatocyte-like cells have mature hepatocyte functions. Furthermore, the hepatocyte-like cells can catalyze the toxication of several compounds (Figure 4e). Although the activities to catalyze the toxication of test compounds in primary human hepatocytes are slightly higher than those in the hepatocyte-like cells, the handling of primary human hepatocytes is difficult for a number of reasons: since their source is limited, large-scale primary human hepatocytes are difficult to prepare as a homogeneous population. Therefore, the hepatocyte-like cells derived from human ESCs and iPSCs would be a valuable tool for predicting drug toxicity. To utilize the hepatocyte-like cells in a drug toxicity study, further investigation of the drug metabolism capacity and CYP induction potency will be needed.

We also investigated the mechanisms underlying efficient hepatic maturation by HNF4α transduction. Although the number of cholangiocyte populations did not change by HNF4α transduction, we found that the number of hepatoblast populations decreased and that of hepatocyte populations increased, indicating that HNF4α promotes selective hepatic differentiation from hepatoblasts (Figure 5a). As previously reported, HNF4α regulates the expression of a broad range of genes that code for cell adhesion molecules,[13] extracellular matrix components, and cytoskeletal proteins, which determine the main morphological characteristics of epithelial cells.[14,35,37] In this study, we elucidated that MET was promoted by HNF4α transduction (Figure 5b,d). Thus, we conclude that HNF4α overexpression in hepatoblasts promotes hepatic differentiation by activating MET (Figure 5e).

Using human iPSCs as well as human ESCs, we confirmed that the stage-specific overexpression of HNF4α could promote hepatic maturation (**Supplementary Figure S9**). Interestingly, the differentiation efficacies differed among human iPS cell lines: two of the human iPS cell lines (Dotcom and Tic) were more committed to the hepatic lineage than another human iPS cell line (201B7) (**Supplementary Figure S7**). Therefore, it would be necessary to select a human iPS cell line that is suitable for hepatic maturation in the case of medical applications, such as drug screening and liver transplantation. The difference of hepatic differentiation efficacy among the three iPSC lines might be due to the difference of epigenetic memory of original cells or the difference of the inserted position of the foreign genes for the reprogramming.

To control hepatic differentiation mimicking embryogenesis, we employed Ad vectors, which are one of the most efficient transient gene delivery vehicles and have been widely used in both experimental studies and clinical trials.[38] We used a fiber-modified Ad vector containing the EF-1α promoter and a stretch of lysine residue (KKKKKKK, K7) peptides in the C-terminal region of the fiber knob.[19] The K7 peptide targets heparan sulfates on the cellular surface, and the fiber-modified Ad vector containing the K7 peptides was shown to be efficient for transduction into many kinds of cells including human ESCs and human ESC-derived cells.[7–8,19] Thus, Ad vector-mediated transient gene transfer should be a powerful tool for regulating cellular differentiation.

In summary, the findings described here demonstrate that transcription factor HNF4α plays a crucial role in the hepatic differentiation from human ESC-derived hepatoblasts by activating MET (Figure 5e). In the present study, both human ESCs and iPSCs (three lines) were used and all cell lines showed efficient hepatic maturation, indicating that our protocol would be a universal tool for cell line-independent differentiation into functional hepatocytes. Moreover, the hepatocyte-like cells can catalyze the toxication of several compounds as primary human hepatocytes. Therefore, our technology, by sequential transduction of SOX17, HEX, and HNF4α, would be a valuable tool for the efficient generation of functional hepatocytes derived from human ESCs and iPSCs, and the hepatocyte-like cells could be used for the prediction of drug toxicity.

MATERIALS AND METHODS

Human ESC and iPSC culture. A human ES cell line, H9 (WiCell Research Institute, Madison, HI), was maintained on a feeder layer of mitomycin C-treated mouse embryonic fibroblasts (Millipore, Billerica, MA) with Repro Stem (Repro CELL, Tokyo, Japan) supplemented with 5 ng/ml fibroblast growth factor 2 (FGF2) (Sigma, St Louis, MO). Human ESCs were dissociated with 0.1 mg/ml dispase (Roche Diagnostics, Indianapolis, IN) into small clumps and then were subcultured every 4 or 5 days. H9 was used following the Guidelines for Derivation and Utilization of Human Embryonic Stem Cells of the Ministry of Education, Culture, Sports, Science and Technology of Japan. Two human iPS cell lines generated from the human embryonic lung fibroblast cell line MCR5 were provided from the JCRB Cell Bank (Tic, JCRB Number: JCRB1331; and Dotcom, JCRB Number: JCRB1327).[39,40] These human iPS cell lines were maintained on a feeder layer of mitomycin C-treated mouse embryonic fibroblasts with iPSellon (Cardio, Kobe, Japan) supplemented with 10 ng/ml FGF2. Another human iPS cell line, 201B7, generated from human dermal fibroblasts was kindly provided by Dr S. Yamanaka (Kyoto University).[2] The human iPS cell line 201B7 was maintained on a feeder layer of mitomycin C-treated mouse embryonic fibroblasts with Repro Stem (Repro CELL) supplemented with 5 ng/ml FGF2 (Sigma). Human iPSCs were dissociated with 0.1 mg/ml dispase (Roche Diagnostics) into small clumps and were then subcultured every 5 or 6 days.

In vitro differentiation. Before the initiation of cellular differentiation, the medium of human ESCs and iPSCs was exchanged for a defined serum-free medium, hESF9, and cultured as we previously reported.[41] hESF9 consists of hESF-GRO medium (Cell Science & Technology Institute, Sendai, Japan) supplemented with 10 μg/ml human recombinant insulin, 5 μg/ml human apotransferrin, 10 μmol/l 2-mercaptoethanol, 10 μmol/l ethanolamine, 10 μmol/l sodium selenite, oleic acid conjugated with fatty-acid-free bovine albumin (BSA), 10 ng/ml FGF2, and 100 ng/ml heparin (all from Sigma).

The differentiation protocol for the induction of DE cells, hepatoblasts, and hepatocytes was based on our previous report with some modifications.[7] Briefly, in mesendoderm differentiation, human ESCs and iPSCs were dissociated into single cells and cultured for 3 days on Matrigel (Becton, Dickinson and Company, Tokyo, Japan) in hESF-DIF medium (Cell Science & Technology Institute) supplemented with 10 μg/ml human recombinant insulin, 5 μg/ml human apotransferrin, 10 μmol/l 2-mercaptoethanol, 10 μmol/l ethanolamine, 10 μmol/l sodium selenite, 0.5 mg/ml BSA, and 100 ng/ml Activin A (R&D Systems, Minneapolis, MN). To generate mesendoderm cells and DE cells, human ESC-derived cells were transduced with 3,000 vector particles (VP)/cell of Ad-SOX17 for 1.5 hours on day 3 and cultured until day 6 on Matrigel (BD) in hESF-DIF medium (Cell Science & Technology Institute) supplemented with 10 μg/ml human recombinant insulin, 5 μg/ml human apotransferrin, 10 μmol/l 2-mercaptoethanol, 10 μmol/l ethanolamine, 10 μmol/l sodium selenite, 0.5 mg/ml BSA, and 100 ng/ml Activin A (R&D Systems). For induction of hepatoblasts, the DE cells were transduced with 3,000 VP/cell of Ad-HEX for 1.5 hours on day 6 and cultured for 3 days on a Matrigel (BD) in hESF-DIF (Cell Science & Technology Institute) medium supplemented with the 10 μg/ml human recombinant insulin, 5 μg/ml human apotransferrin, 10 μmol/l 2-mercaptoethanol, 10 μmol/l ethanolamine, 10 μmol/l sodium selenite, 0.5 mg/ml BSA, 20 ng/ml bone morphogenetic protein 4 (R&D Systems), and 20 ng/ml FGF4 (R&D Systems). In hepatic differentiation, hepatoblasts were transduced with 3,000 VP/cell of Ad-LacZ or Ad-HNF4α for 1.5 hr on day 9 and were cultured for 11 days on Matrigel (BD) in L15 medium (Invitrogen, Carlsbad, CA) supplemented with 8.3% tryptose phosphate broth (BD), 8.3% fetal bovine serum (Vita, Chiba, Japan), 10 μmol/l hydrocortisone 21-hemisuccinate (Sigma), 1 μmol/l insulin, 25 mmol/l $NaHCO_3$ (Wako, Osaka, Japan), 20 ng/ml hepatocyte growth factor (R&D Systems), 20 ng/ml Oncostatin M (R&D Systems), and 10^{-6} mol/l Dexamethasone (Sigma).

Ad vectors. Ad vectors were constructed by an improved *in vitro* ligation method.[42,43] The human HNF4α gene (accession number NM_000457) was amplified by PCR using primers designed to incorporate the 5′ Not I and 3′ Xba I restriction enzyme sites: Fwd 5′-ggcctctagatggaggcagggagaatg-3′ and Rev 5′-ccccgcggccgcagcggcttgctagataac-3′. The human HNF4α gene was inserted into pBSKII (Invitrogen), resulting in pBSKII-HNF4α, and then the human HNF4α gene was inserted into pHMEF5,[44] which contains the human elongation factor-1α (EF-1α) promoter, resulting in pHMEF-HNF4α. The pHMEF-HNF4α was digested with I-CeuI/PI-SceI and ligated into I-Ceu I/PI-SceI-digested pAdHM41-K7,[19] resulting in pAd-HNF4α. The human EF-1α promoter-driven LacZ-, SOX17-, or HEX-expressing Ad vectors, Ad-LacZ, Ad-SOX17, or Ad-HEX, were constructed previously.[7,8,45] Ad-LacZ, Ad-SOX17, Ad-HEX, and Ad-HNF4α, each of which contains a stretch of lysine residue (K7) peptides in the C-terminal region of the fiber knob for more efficient transduction of human ESCs, iPSCs, and DE cells, were generated and purified as described previously.[7] The VP titer was determined by using a spectrophotometric method.[46]

LacZ assay. Human ESC- and iPSC-derived cells were transduced with Ad-LacZ at 3,000 VP/cell for 1.5 hours. After culturing for the indicated number of days, 5-bromo-4-chloro-3-indolyl β-D-galactopyranoside (X-Gal) staining was performed as described previously.[44]

Flow cytometry. Single-cell suspensions of human ESCs, iPSCs, and their derivatives were fixed with methanol at 4 °C for 20 minutes and then incubated with the primary antibody, followed by the secondary antibody. Flow cytometry analysis was performed using a FACS LSR Fortessa flow cytometer (BD).

RNA isolation and reverse transcription-PCR. Total RNA was isolated from human ESCs, iPSCs, and their derivatives using ISOGENE (Nippon Gene) according to the manufacturer's instructions. Primary human hepatocytes were purchased from CellzDirect, Durham, NC. complementary DNA was synthesized using 500 ng of total RNA with a Superscript VILO cDNA synthesis kit (Invitrogen). Real-time reverse transcription-PCR was performed with Taqman gene expression assays (Applied Biosystems, Foster City, CA) or SYBR Premix Ex Taq (TaKaRa) using an ABI PRISM 7000 Sequence Detector (Applied Biosystems). Relative quantification was performed against a standard curve and the values were normalized against the input determined for the housekeeping gene, glyceraldehyde 3-phosphate dehydrogenase. The primer sequences used in this study are described in **Supplementary Table S1**.

Immunohistochemistry. The cells were fixed with methanol or 4% paraformaldehyde (Wako). After blocking with phosphate-buffered saline containing 2% BSA (Sigma) and 0.2% Triton X-100 (Sigma), the cells were incubated with primary antibody at 4 °C for 16 hours, followed by incubation with a secondary antibody that was labeled with Alexa Fluor 488 (Invitrogen) or Alexa Fluor 594 (Invitrogen) at room temperature for 1 hour. All the antibodies are listed in **Supplementary Table S2**.

Assay for CYP activity. To measure cytochrome P450 3A4, 2C9, and 1A2 activity, we performed Lytic assays by using a P450-GloTM CYP3A4 Assay Kit (Promega, Madison, WI). For the CYP3A4 and 2C9 activity assay, undifferentiated human ESCs, the hepatocyte-like cells, and primary human hepatocytes were treated with rifampicin (Sigma), which is the substrate for CYP3A4 and CYP2C9, at a final concentration of 25 μmol/l or DMSO (0.1%) for 48 hours. For the CYP1A2 activity assay, undifferentiated human ESCs, the hepatocyte-like cells, and primary human hepatocytes were treated with omeprazole (Sigma), which is the substrate for CYP1A2, at a final concentration of 10 μM or DMSO (0.1%) for 48 hours. We measured the fluorescence activity with a luminometer (Lumat LB 9507; Berthold, Oak Ridge, TN) according to the manufacturer's instructions.

Pyronin Y/Hoechst Staining. Human ESC-derived cells were stained with Hoechst33342 (Sigma) and Pyronin Y (PY) (Sigma) in Dulbecco's modified Eagle medium (Wako) supplemented with 0.2 mmol/l HEPES and 5% FCS (Invitrogen). Samples were then placed on ice for 15 minutes, and 7-AAD was added to a final concentration of 0.5 mg/ml for exclusion of dead cells. Fluorescence-activated cell-sorting analysis of these cells was performed on a FACS LSR Fortessa flow cytometer (Becton Dickinson) equipped with a UV-laser.

Cellular uptake and excretion of ICG. ICG (Sigma) was dissolved in DMSO at 100 mg/ml, then added to a culture medium of the hepatocyte-like cells to a final concentration of 1 mg/ml on day 20 of differentiation. After incubation at 37 °C for 60 minutes, the medium with ICG was discarded and the cells were washed with phosphate-buffered saline. The cellular uptake of ICG was then examined by microscopy. Phosphate-buffered saline was then replaced by the culture medium and the cells were incubated at 37 °C for 6 hours. The excretion of ICG was examined by microscopy.

Periodic Acid-Schiff assay for glycogen. The hepatocyte-like cells were fixed with 4% paraformaldehyde and stained using a Periodic Acid-Schiff staining system (Sigma) on day 20 of differentiation according to the manufacturer's instructions.

Cell viability tests. Cell viability was assessed by Alamar Blue assay kit (Invitrogen). After treatment with test compounds[47–50] (troglitazone, acetaminophen, cyclophosphamide, and carbamazepine) (all from Wako) for 2 days, the culture medium was replaced with 0.5 mg/ml solution of Alamar Blue in culturing medium and cells were incubated for 3 hours at 37 °C. The supernatants of the cells were measured at a wavelength of 570 nm with background subtraction at 600 nm in a plate reader. Control refers to incubations in the absence of test compounds and was considered as 100% viability value.

Uptake of LDL. The hepatocyte-like cells were cultured with medium containing Alexa-488-labeled LDL (Invitrogen) for 1 hour, and then the cells that could uptake LDL were assessed by immunohistochemistry and flow cytometry.

Primary human hepatocytes. Cryopreserved human hepatocytes were purchased from CellzDirect (lot Hu8072). The vials of hepatocytes were rapidly thawed in a shaking water bath at 37 °C; the contents of the vial were emptied into prewarmed Cryopreserved Hepatocyte Recovery Medium (CellzDirect) and the suspension was centrifuged at 100*g* for 10 minutes at room temperature. The hepatocytes were seeded at 1.25×10^5 cells/cm^2 in hepatocyte culture medium (Lonza, Walkersville, MD) containing 10% FCS (GIBCO-BRL) onto type I collagen-coated 12-well plates. The medium was replaced with hepatocyte culture medium containing 10% FCS (GIBCO-BRL) 6 hours after seeding. The hepatocytes, which were cultured 48 hours after plating the cells, were used in the experiments.

SUPPLEMENTARY MATERIAL

Figure S1. Genome-wide screening of transcription factors involved in hepatic differentiation emphasizes the importance of the transcription factor HNF4α.
Figure S2. Summary of specific markers for DE cells, hepatoblasts, hepatocytes, cholangiocytes, and pancreas cells.
Figure S3. The formation of DE cells, hepatoblasts, hepatocytes, and cholangiocytes from human ESCs.
Figure S4. Overexpression of HNF4α mRNA in hepatoblasts by Ad-HNF4α transduction.
Figure S5. Time course of LacZ expression in hepatoblasts transduced with Ad-LacZ.
Figure S6. The morphology of the hepatocyte-like cells.
Figure S7. Upregulation of the expression levels of conjugating enzymes and hepatic transporters by HNF4α transduction.
Figure S8. Upregulation of the expression levels of hepatic transcription factors by HNF4α transduction.
Figure S9. Generation of hepatocytes from various human ES or iPS cell lines.
Figure S10. Promotion of MET by HNF4α transduction.
Figure S11. Arrest of cell growth by HNF4α transduction.
Table S1. List of Taqman probes and primers used in this study.
Table S2. List of antibodies used in this study.

ACKNOWLEDGMENTS

We thank Hiroko Matsumura and Misae Nishijima for their excellent technical support. H.M., M.K.F., and T.H. were supported by grants from the Ministry of Health, Labor, and Welfare of Japan. H.M. was also supported by Japan Research foundation For Clinical Phamacology, The Nakatomi Foundation, and The Uehara Memorial Foundation. K.K. (K. Kawabata) was supported by grants from the Ministry of Education, Sports, Science and Technology of Japan (20200076) and the Ministry of Health, Labor, and Welfare of Japan. K.K. (K. Katayama) and F.S. was supported by Program for Promotion of Fundamental Studies in Health Sciences of the National Institute of Biomedical Innovation (NIBIO).

REFERENCES

1. Thomson, JA, Itskovitz-Eldor, J, Shapiro, SS, Waknitz, MA, Swiergiel, JJ, Marshall, VS *et al.* (1998). Embryonic stem cell lines derived from human blastocysts. *Science* **282**: 1145–1147.
2. Takahashi, K, Tanabe, K, Ohnuki, M, Narita, M, Ichisaka, T, Tomoda, K *et al.* (2007). Induction of pluripotent stem cells from adult human fibroblasts by defined factors. *Cell* **131**: 861–872.
3. Murry, CE and Keller, G (2008). Differentiation of embryonic stem cells to clinically relevant populations: lessons from embryonic development. *Cell* **132**: 661–680.
4. Basma, H, Soto-Gutiérrez, A, Yannam, GR, Liu, L, Ito, R, Yamamoto, T *et al.* (2009). Differentiation and transplantation of human embryonic stem cell-derived hepatocytes. *Gastroenterology* **136**: 990–999.
5. Touboul, T, Hannan, NR, Corbineau, S, Martinez, A, Martinet, C, Branchereau, S *et al.* (2010). Generation of functional hepatocytes from human embryonic stem cells under chemically defined conditions that recapitulate liver development. *Hepatology* **51**: 1754–1765.
6. Duan, Y, Ma, X, Ma, X, Zou, W, Wang, C, Bahbahan, IS *et al.* (2010). Differentiation and characterization of metabolically functioning hepatocytes from human embryonic stem cells. *Stem Cells* **28**: 674–686.
7. Inamura, M, Kawabata, K, Takayama, K, Tashiro, K, Sakurai, F, Katayama, K *et al.* (2011). Efficient generation of hepatoblasts from human ES cells and iPS cells by transient overexpression of homeobox gene HEX. *Mol Ther* **19**: 400–407.
8. Takayama, K, Inamura, M, Kawabata, K, Tashiro, K, Katayama, K, Sakurai, F *et al.* (2011). Efficient and directive generation of two distinct endoderm lineages from human ESCs and iPSCs by differentiation stage-specific SOX17 transduction. *PLoS ONE* **6**: e21780.
9. Duncan, SA, Manova, K, Chen, WS, Hoodless, P, Weinstein, DC, Bachvarova, RF *et al.* (1994). Expression of transcription factor HNF-4 in the extraembryonic endoderm, gut, and nephrogenic tissue of the developing mouse embryo: HNF-4 is a marker for primary endoderm in the implanting blastocyst. *Proc Natl Acad Sci USA* **91**: 7598–7602.
10. Taraviras, S, Monaghan, AP, Schütz, G and Kelsey, G (1994). Characterization of the mouse HNF-4 gene and its expression during mouse embryogenesis. *Mech Dev* **48**: 67–79.
11. Parviz, F, Matullo, C, Garrison, WD, Savatski, L, Adamson, JW, Ning, G *et al.* (2003). Hepatocyte nuclear factor 4alpha controls the development of a hepatic epithelium and liver morphogenesis. *Nat Genet* **34**: 292–296.
12. Odom, DT, Zizlsperger, N, Gordon, DB, Bell, GW, Rinaldi, NJ, Murray, HL *et al.* (2004). Control of pancreas and liver gene expression by HNF transcription factors. *Science* **303**: 1378–1381.
13. Battle, MA, Konopka, G, Parviz, F, Gaggl, AL, Yang, C, Sladek, FM *et al.* (2006). Hepatocyte nuclear factor 4alpha orchestrates expression of cell adhesion proteins during the epithelial transformation of the developing liver. *Proc Natl Acad Sci USA* **103**: 8419–8424.
14. Konopka, G, Tekiela, J, Iverson, M, Wells, C and Duncan, SA (2007). Junctional adhesion molecule-A is critical for the formation of pseudocanaliculi and modulates E-cadherin expression in hepatic cells. *J Biol Chem* **282**: 28137–28148.
15. Li, J, Ning, G and Duncan, SA (2000). Mammalian hepatocyte differentiation requires the transcription factor HNF-4alpha. *Genes Dev* **14**: 464–474.
16. Hayhurst, GP, Lee, YH, Lambert, G, Ward, JM and Gonzalez, FJ (2001). Hepatocyte nuclear factor 4alpha (nuclear receptor 2A1) is essential for maintenance of hepatic gene expression and lipid homeostasis. *Mol Cell Biol* **21**: 1393–1403.
17. Khurana, S, Jaiswal, AK and Mukhopadhyay, A (2010). Hepatocyte nuclear factor-4alpha induces transdifferentiation of hematopoietic cells into hepatocytes. *J Biol Chem* **285**: 4725–4731.
18. Suetsugu, A, Nagaki, M, Aoki, H, Motohashi, T, Kunisada, T and Moriwaki, H (2008). Differentiation of mouse hepatic progenitor cells induced by hepatocyte nuclear factor-4 and cell transplantation in mice with liver fibrosis. *Transplantation* **86**: 1178–1186.
19. Koizumi, N, Mizuguchi, H, Utoguchi, N, Watanabe, Y and Hayakawa, T (2003). Generation of fiber-modified adenovirus vectors containing heterologous peptides in both the HI loop and C terminus of the fiber knob. *J Gene Med* **5**: 267–276.
20. Shiojiri, N (1984). The origin of intrahepatic bile duct cells in the mouse. *J Embryol Exp Morphol* **79**: 25–39.
21. Moll, R, Franke, WW, Schiller, DL, Geiger, B and Krepler, R (1982). The catalog of human cytokeratins: patterns of expression in normal epithelia, tumors and cultured cells. *Cell* **31**: 11–24.

22. Antoniou, A, Raynaud, P, Cordi, S, Zong, Y, Tronche, F, Stanger, BZ *et al.* (2009). Intrahepatic bile ducts develop according to a new mode of tubulogenesis regulated by the transcription factor SOX9. *Gastroenterology* **136**: 2325–2333.
23. Offield, MF, Jetton, TL, Labosky, PA, Ray, M, Stein, RW, Magnuson, MA *et al.* (1996). PDX-1 is required for pancreatic outgrowth and differentiation of the rostral duodenum. *Development* **122**: 983–995.
24. Sussel, L, Kalamaras, J, Hartigan-O'Connor, DJ, Meneses, JJ, Pedersen, RA, Rubenstein, JL *et al.* (1998). Mice lacking the homeodomain transcription factor Nkx2.2 have diabetes due to arrested differentiation of pancreatic beta cells. *Development* **125**: 2213–2221.
25. Ingelman-Sundberg, M, Oscarson, M and McLellan, RA (1999). Polymorphic human cytochrome P450 enzymes: an opportunity for individualized drug treatment. *Trends Pharmacol Sci* **20**: 342–349.
26. Henderson, CJ, Otto, DM, Carrie, D, Magnuson, MA, McLaren, AW, Rosewell, I *et al.* (2003). Inactivation of the hepatic cytochrome P450 system by conditional deletion of hepatic cytochrome P450 reductase. *J Biol Chem* **278**: 13480–13486.
27. Yamada, T, Yoshikawa, M, Kanda, S, Kato, Y, Nakajima, Y, Ishizaka, S *et al.* (2002). *In vitro* differentiation of embryonic stem cells into hepatocyte-like cells identified by cellular uptake of indocyanine green. *Stem Cells* **20**: 146–154.
28. Anzenbacher, P and Anzenbacherová, E (2001). Cytochromes P450 and metabolism of xenobiotics. *Cell Mol Life Sci* **58**: 737–747.
29. Zhao, D, Chen, S, Cai, J, Guo, Y, Song, Z, Che, J *et al.* (2009). Derivation and characterization of hepatic progenitor cells from human embryonic stem cells. *PLoS ONE* **4**: e6468.
30. Hatta, K, Takagi, S, Fujisawa, H and Takeichi, M (1987). Spatial and temporal expression pattern of N-cadherin cell adhesion molecules correlated with morphogenetic processes of chicken embryos. *Dev Biol* **120**: 215–227.
31. Shiojiri, N (1981). Enzymo- and immunocytochemical analyses of the differentiation of liver cells in the prenatal mouse. *J Embryol Exp Morphol* **62**: 139–152.
32. Lee, JM, Dedhar, S, Kalluri, R and Thompson, EW (2006). The epithelial-mesenchymal transition: new insights in signaling, development, and disease. *J Cell Biol* **172**: 973–981.
33. Macleod, KF, Sherry, N, Hannon, G, Beach, D, Tokino, T, Kinzler, K *et al.* (1995). p53-dependent and independent expression of p21 during cell growth, differentiation, and DNA damage. *Genes Dev* **9**: 935–944.
34. Si-Tayeb, K, Noto, FK, Nagaoka, M, Li, J, Battle, MA, Duris, C *et al.* (2010). Highly efficient generation of human hepatocyte-like cells from induced pluripotent stem cells. *Hepatology* **51**: 297–305.
35. Sekiya, S and Suzuki, A (2011). Direct conversion of mouse fibroblasts to hepatocyte-like cells by defined factors. *Nature* **475**: 390–393.
36. Huang, P, He, Z, Ji, S, Sun, H, Xiang, D, Liu, C *et al.* (2011). Induction of functional hepatocyte-like cells from mouse fibroblasts by defined factors. *Nature* **475**: 386–389.
37. Satohisa, S, Chiba, H, Osanai, M, Ohno, S, Kojima, T, Saito, T *et al.* (2005). Behavior of tight-junction, adherens-junction and cell polarity proteins during HNF-4alpha-induced epithelial polarization. *Exp Cell Res* **310**: 66–78.
38. Xu, ZL, Mizuguchi, H, Sakurai, F, Koizumi, N, Hosono, T, Kawabata, K *et al.* (2005). Approaches to improving the kinetics of adenovirus-delivered genes and gene products. *Adv Drug Deliv Rev* **57**: 781–802.
39. Nagata, S, Toyoda, M, Yamaguchi, S, Hirano, K, Makino, H, Nishino, K *et al.* (2009). Efficient reprogramming of human and mouse primary extra-embryonic cells to pluripotent stem cells. *Genes Cells* **14**: 1395–1404.
40. Makino, H, Toyoda, M, Matsumoto, K, Saito, H, Nishino, K, Fukawatase, Y *et al.* (2009). Mesenchymal to embryonic incomplete transition of human cells by chimeric OCT4/3 (POU5F1) with physiological co-activator EWS. *Exp Cell Res* **315**: 2727–2740.
41. Furue, MK, Na, J, Jackson, JP, Okamoto, T, Jones, M, Baker, D *et al.* (2008). Heparin promotes the growth of human embryonic stem cells in a defined serum-free medium. *Proc Natl Acad Sci USA* **105**: 13409–13414.
42. Mizuguchi, H and Kay, MA (1998). Efficient construction of a recombinant adenovirus vector by an improved *in vitro* ligation method. *Hum Gene Ther* **9**: 2577–2583.
43. Mizuguchi, H and Kay, MA (1999). A simple method for constructing E1- and E1/E4-deleted recombinant adenoviral vectors. *Hum Gene Ther* **10**: 2013–2017.
44. Kawabata, K, Sakurai, F, Yamaguchi, T, Hayakawa, T and Mizuguchi, H (2005). Efficient gene transfer into mouse embryonic stem cells with adenovirus vectors. *Mol Ther* **12**: 547–554.
45. Tashiro, K, Kawabata, K, Sakurai, H, Kurachi, S, Sakurai, F, Yamanishi, K *et al.* (2008). Efficient adenovirus vector-mediated PPAR gamma gene transfer into mouse embryoid bodies promotes adipocyte differentiation. *J Gene Med* **10**: 498–507.
46. Maizel, JV Jr, White, DO and Scharff, MD (1968). The polypeptides of adenovirus. I. Evidence for multiple protein components in the virion and a comparison of types 2, 7A, and 12. *Virology* **36**: 115–125.
47. Smith, MT (2003). Mechanisms of troglitazone hepatotoxicity. *Chem Res Toxicol* **16**: 679–687.
48. Dai, Y and Cederbaum, AI (1995). Cytotoxicity of acetaminophen in human cytochrome P4502E1-transfected HepG2 cells. *J Pharmacol Exp Ther* **273**: 1497–1505.
49. Chang, TK, Weber, GF, Crespi, CL and Waxman, DJ (1993). Differential activation of cyclophosphamide and ifosphamide by cytochromes P-450 2B and 3A in human liver microsomes. *Cancer Res* **53**: 5629–5637.
50. Miao, XS and Metcalfe, CD (2003). Determination of carbamazepine and its metabolites in aqueous samples using liquid chromatography-electrospray tandem mass spectrometry. *Anal Chem* **75**: 3731–3738.

nature COMMUNICATIONS

ARTICLE

Received 10 Sep 2012 | Accepted 24 Jan 2013 | Published 26 Feb 2013 DOI: 10.1038/ncomms2540 OPEN

GRK6 deficiency in mice causes autoimmune disease due to impaired apoptotic cell clearance

Michio Nakaya[1], Mitsuru Tajima[1], Hidetaka Kosako[2], Takeo Nakaya[3], Akiko Hashimoto[1], Kenji Watari[1], Hiroaki Nishihara[1], Mina Ohba[1], Shiori Komiya[1], Naoki Tani[2], Motohiro Nishida[1], Hisaaki Taniguchi[2], Yoji Sato[4], Mitsuru Matsumoto[5], Makoto Tsuda[6], Masahiko Kuroda[3], Kazuhide Inoue[6] & Hitoshi Kurose[1]

Efficient engulfment of apoptotic cells is critical for maintaining tissue homoeostasis. When phagocytes recognize 'eat me' signals presented on the surface of apoptotic cells, this subsequently induces cytoskeletal rearrangement of phagocytes for the engulfment through Rac1 activation. However, the intracellular signalling cascades that result in Rac1 activation remain largely unknown. Here we show that G-protein-coupled receptor kinase 6 (GRK6) is involved in apoptotic cell clearance. GRK6 cooperates with GIT1 to activate Rac1, which promotes apoptotic engulfment independently from the two known DOCK180/ELMO/Rac1 and GULP1/Rac1 engulfment pathways. As a consequence, GRK6-deficient mice develop an autoimmune disease. GRK6-deficient mice also have increased iron stores in splenic red pulp in which F4/80^{+} macrophages are responsible for senescent red blood cell clearance. Our results reveal previously unrecognized roles for GRK6 in regulating apoptotic engulfment and its fundamental importance in immune and iron homoeostasis.

---

[1] Department of Pharmacology and Toxicology, Graduate School of Pharmaceutical Sciences, Kyushu University, Fukuoka 812-8582, Japan. [2] Division of Disease Proteomics, Institute for Enzyme Research, University of Tokushima, Tokushima 770-8503, Japan. [3] Department of Molecular Pathology, Tokyo Medical University, Tokyo 160-8402, Japan. [4] Division of Cellular and Gene Therapy Products, National Institute of Health Sciences, Setagaya, Tokyo 158-8501, Japan. [5] Division of Molecular Immunology, Institute for Enzyme Research, University of Tokushima, Tokushima 770-8503, Japan. [6] Molecular and System Pharmacology, Graduate School of Pharmaceutical Sciences, Kyushu University, Fukuoka 812-8582, Japan. Correspondence and requests for materials should be addressed to H.K. (email: kurose@phar.kyushu-u.ac.jp).

During animal development and in immune responses, numerous harmful and unnecessary cells are generated. These cells undergo apoptosis and are rapidly engulfed by phagocytes such as macrophages and dendritic cells. When an engulfment system does not function adequately, dying cells accumulate and undergo secondary necrosis that results in the release of noxious cellular components into the extracellular space. These released self-antigens are considered to induce lymphocyte activation and autoantibody production, which results in the development of autoimmune diseases such as systemic lupus erythematosus (SLE). Thus, the efficient clearance of apoptotic cells is indispensable for maintaining tissue homoeostasis. Apoptotic cell removal is supposedly triggered by the release of 'find me' signals such as nucleotides and lipids from dying cells[1]. These signals recruit phagocytes to the apoptotic cells. Subsequently, the recruited phagocytes recognize 'eat me' signals on the surface of apoptotic cells through the corresponding phagocyte receptors[2]. This receptor recognition then elicits signals that induce cytoskeletal rearrangements for encapsulating the apoptotic cells[3].

To date, a variety of ligands on apoptotic cells and their corresponding receptors on phagocytes have been proposed to be involved in this recognition process[4]. Two conserved intracellular pathways, CrkII/DOCK180/ELMO/Rac1 and GULP/Rac1, are well known to be involved in cytoskeletal rearrangements for apoptotic cell engulfment[5–7]. However, molecules downstream of phagocytic receptors that are required for ingesting apoptotic cells still remain much to be determined.

G-protein-coupled receptor kinase 6 (GRK6) is a member of the GRK superfamily. GRKs were initially identified as molecules that phosphorylate G-protein-coupled receptors (GPCRs) and result in their desensitization[8–10]. When GPCRs are activated by binding to their cognate ligands, GRKs recognize these activated receptors and phosphorylate them. Then, β-arrestins bind to these phosphorylated receptors, which block further stimulation of G-proteins by the agonist-bound receptors through steric hindrance[11]. In addition to regulating GPCR desensitization, recent evidence indicates that GRKs have roles in cellular signalling independently of the GPCR-mediated pathways by phosphorylating non-GPCR substrates[12,13]. For example, GRK2 and GRK5 phosphorylate IRS1 and HDAC5, respectively[14,15]. Although numerous *in vitro* studies have established the importance of GRKs for regulating GPCR signalling and phosphorylating non-GPCR proteins, the physiological and pathological roles of GRKs, including GRK6, *in vivo* remain poorly understood.

Here we demonstrate a previously unknown function for GRK6 in apoptotic cell clearance. GRK6 enhances apoptotic cell engulfment through Rac1 activation, an indispensable molecule involved in engulfment signalling. In addition, we show that this GRK6-mediated engulfment depends on GIT1[16] and phosphorylation of radixin and moesin[17], both of which have been implicated in membrane skeleton organization. GRK6-deficient macrophages exhibited impaired phagocytosis of apoptotic cells. Consequently, GRK6-deficient mice developed an autoimmune condition similar to those of mice with other knocked-out molecules involved in apoptotic engulfment. We also found that GRK6 was highly expressed in red splenic macrophages responsible for removing senescent red blood cells. GRK6 significantly contributed to their clearance, as GRK6-deficient mice had increased iron stores because of the inefficient iron uptake in the red pulp of their spleens. Our results establish that GRK6 is a critical factor for regulating immune and iron homoeostasis.

Results

GRK6 is involved in the engulfment of apoptotic cells. To examine the possible involvement of GRK family members in the engulfment of apoptotic cells, we first examined the effects of GRKs on the engulfment by NIH3T3 cells. NIH3T3 is a mouse embryonic fibroblast cell line, although these cells can engulf apoptotic thymocytes. In addition, the efficiency of retroviral gene transfer to these cells is >90%. Thus, we used NIH3T3 cells as phagocytes in our experiments. Among the seven GRKs, some GRK (GRK1, 4 and 7) expressions are restricted to certain tissues, whereas other GRKs (GRK2, 3, 5 and 6) are widely expressed[18]. Thus, we introduced kinase-inactive and dominant-negative (DN) mutants[19] of GRK2, 3, 5 and 6 (GRK2 (K220R), GRK3 (K220R), GRK5 (K215R) and GRK6 (K215R)) into NIH3T3 cells and determined the effect of each mutant on NIH3T3 cells' engulfment capacity. Virally infected NIH3T3 cells were co-cultured with fluorescently labelled apoptotic thymocytes at 37 °C for 90 min. After co-culture, the fluorescence uptake by NIH3T3 cells was evaluated by flow cytometry. As shown in Fig. 1a, 18% of the vector-expressing NIH3T3 cells engulfed apoptotic cells under these experimental conditions. Among the four kinase-inactive and DN GRK mutants, only GRK6 (K215R) significantly attenuated apoptotic cell engulfment by NIH3T3 cells, which indicated that GRK6 kinase activity was important for efficient engulfment (Fig. 1a). Knockdown of GRK6 by small interfering RNA (siRNA) treatment (about 70% reductions in the GRK6 protein level) also reduced the engulfment by NIH3T3 cells (Fig. 1b). Conversely, overexpression of GRK6 increased engulfment by NIH3T3 cells (Fig. 1c). These results demonstrated that GRK6 enhanced the clearance of apoptotic cells. In contrast to GRK6, GRK2 (K220R) expression increased apoptotic engulfment (Fig. 1a). However, GRK2 knockdown by siRNA resulted in significantly decreased engulfment, and overexpression of GRK2 greatly increased engulfment (Supplementary Fig. S1). These results indicated that GRK2 could enhance engulfment independent of its kinase activity, which is similar to the role of GRK2 in cell migration[20].

Next, we examined if GRK6 mediated apoptotic cell engulfment by macrophages. Bone marrow-derived macrophages (BMDMs) from wild-type (WT) mice expressed GRK6 (Supplementary Fig. S2) and efficiently engulfed apoptotic thymocytes. In comparison, BMDMs from GRK6-deficient mice had a significantly decreased ability to engulf apoptotic cells (Fig. 1d). GRK6-deficient BMDMs also had decreased uptake of fluorescent microspheres, although the extent of this decrease was less than that observed for apoptotic cell engulfment (Supplementary Fig. S3).

We further examined the contribution of GRK6 to apoptotic cell clearance by macrophages *in vivo*. Fluorescently labelled apoptotic thymocytes were injected into WT and GRK6-deficient mice. Phagocytosis by splenic macrophages from GRK6-deficient mice was approximately one-third less than that by macrophages from WT mice, which indicated that engulfment was impaired in GRK6-deficient splenic macrophages (Fig. 1e). Collectively, GRK6 contributes to the efficient engulfment of apoptotic cells in various types of phagocytes, including macrophages.

GRK6 operates upstream of Rac1 for engulfment. To determine the molecular mechanisms by which GRK6 enhances apoptotic engulfment, we examined whether Rac1 participated in the GRK6-mediated engulfment pathway. Rac1 is an indispensable molecule for apoptotic cell engulfment[3]. Consistent with the results of a previous study[21], a DN Rac1 mutant, Rac1 (T17N), almost completely inhibited engulfment by NIH3T3 cells. WT Rac1 expression markedly enhanced engulfment, which confirmed Rac1's indispensable role in engulfment (Fig. 2a). Next, we co-expressed WT GRK6 and DN Rac1, Rac1 (T17N). Rac1 (T17N) expression completely abolished the enhanced

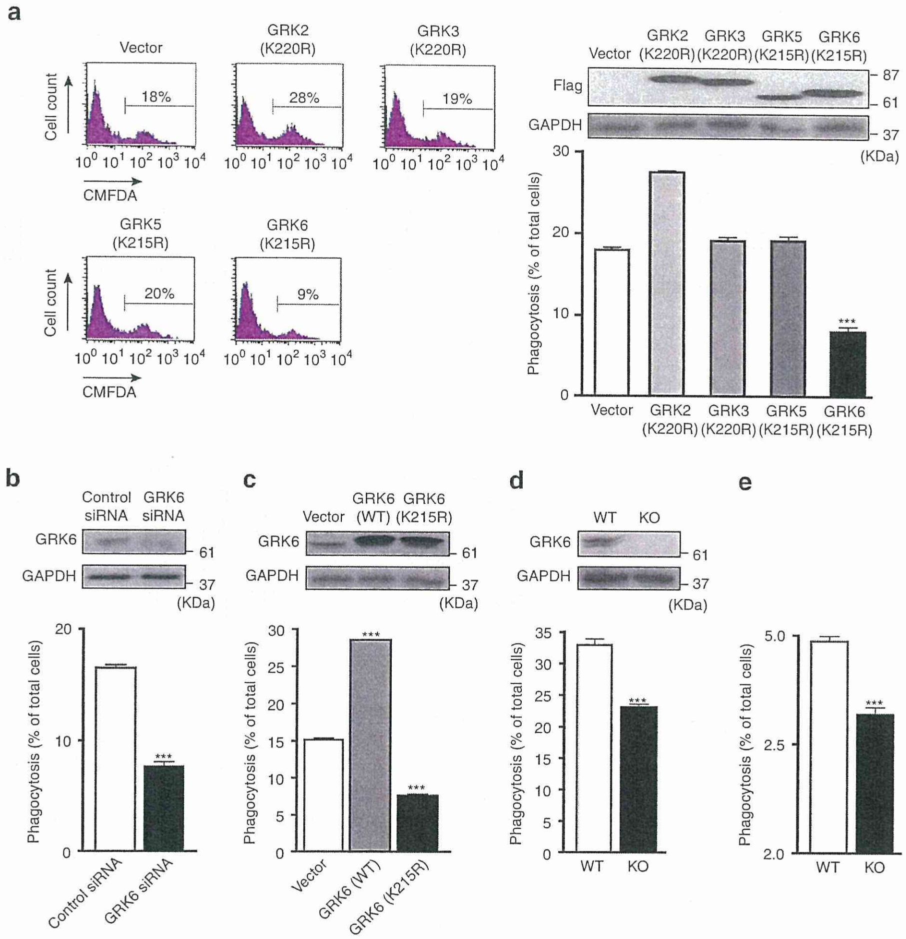

Figure 1 | Involvement of GRK6 in the engulfment of apoptotic cells. (**a**) NIH3T3 cells were infected with the empty retrovirus vector or the virus carrying the cDNA for kinase-inactive form of GRK2, GRK3, GRK5 or GRK6 (GRK2 (K220R), GRK3 (K220R), GRK5 (K215R) or GRK6 (K215R)) with N-terminal Flag tag. The infected cells (4×10^4 cells) were co-cultured with CMFDA-labelled WT thymocytes (1×10^6 cells) at 37 °C for 90 min. Percentages of the phagocytes carrying the engulfed thymocytes were determined by FACS as detailed in Methods. The representative FACS profiles with the NIH3T3 cells expressing GRK2 (K220R), GRK3 (K220R), GRK5 (K215R) or GRK6 (K215R) are shown from four independent experiments performed in triplicate. The expression level of each GRK mutant in NIH3T3 cells was determined by immunoblot analysis using anti-Flag and anti-GAPDH antibodies. (**b**) The engulfment ability of NIH3T3 cells transfected with control or GRK6 siRNA was estimated by FACS analysis as described in **a**. The cell lysates of the NIH3T3 cells were analysed by western blot with antibody against GRK6 or GAPDH. Expression level of GRK6 was decreased to about 30% of the normal level following treatment with GRK6 siRNA. (**c**) The engulfment ability of NIH3T3 cells expressing GRK6 (WT) or GRK6 (K215R) was evaluated by FACS as described in **a**. The level of GRK6 (WT) or GRK6 (K215R) was more than 10-fold greater than endogenous levels, determined by immunoblot using anti-GRK6 antibody. (**d**) BMDMs (1×10^5 cells) from WT and GRK6-deficient mice were co-cultured with CMFDA-labelled apoptotic thymocytes (1×10^6 cells) at 37 °C for 60 min. The percentage of the phagocytes carrying the engulfed thymocytes is presented. BMDM lysates from WT and GRK6-deficient mice were analysed by western blot with antibody against GRK6 or GAPDH. (**e**) CMFDA-labelled apoptotic thymocytes (8×10^7 cells) were injected to WT and GRK6-deficient mice from tail vein. Two hours after the injection, their spleens were isolated and stained with anti-CD11b antibody. Percentage of CD11b$^+$ splenic macrophage carrying the labelled thymocytes was evaluated by flow cytometer. All the experiments were done at least three times; all graphs show average with s.e.m. ***$P < 0.001$. KO, knockout.

engulfment induced by GRK6 (Fig. 2a). In contrast, GRK6 (K215R) expression did not significantly affect Rac1-promoted engulfment (Fig. 2b). The formation of lamellipodia that is characteristic for Rac1 activation[22] was observed in GRK6-expressing cells, whereas GRK6 (K215R) and Rac1 (T17N) expression significantly attenuated the formation of lamellipodia (Supplementary Fig. S4). These morphological results together with our other data regarding engulfment suggested that GRK6 activated Rac1. We next examined the effect of GRK6 on Rac1 activity using a pull-down assay with the Rac1-binding domain of PAK (PAK-RBD), which specifically binds to the GTP form of Rac1. As shown in Fig. 2c, this pull-down assay showed that GRK6 overexpression significantly increased the level of Rac1-GTP, whereas the expression of GRK6 (K215R) decreased it. These results indicated that GRK6 enhanced engulfment through Rac1 activation.

GRK6 is part of a novel engulfment pathway. The best-known and best-established intracellular molecular pathways involved in engulfment are the DOCK180/ELMO/Rac1 and GULP/Rac1 pathways, which have been identified in *Caenorhabditis elegans* and are conserved in mammals. These pathways supposedly operate in parallel, although in a partially redundant manner[5].

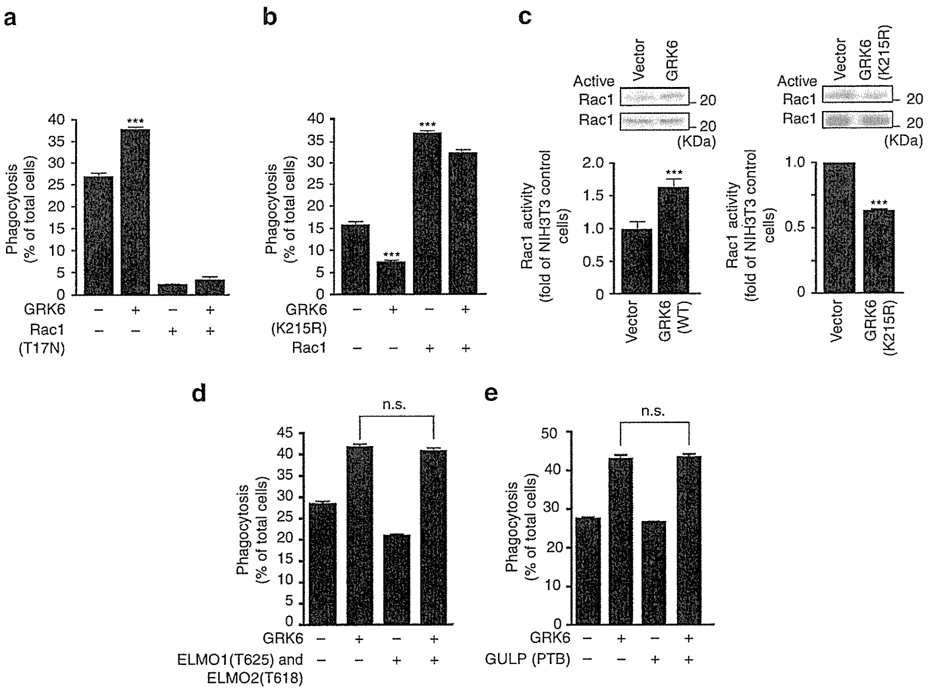

Figure 2 | GRK6 regulates engulfment of apoptotic cells via Rac1. (**a**,**b**) NIH3T3 cells were infected with retroviruses encoding WT GRK6 and DN Rac1 (T17N) (**a**), or kinase-inactive GRK6 (K215R) and WT Rac1 (**b**), either alone or in combination. The infected cells were subjected to the engulfment assay with CMFDA-labelled WT thymocytes. Percentages of the phagocytes carrying the engulfed thymocytes were determined by FACS. (**c**) NIH3T3 cells infected with the empty retrovirus vector or the virus carrying the cDNA for WT GRK6 were subjected to GTP-Rac1 pull-down assay using GST-CRIB. The pull-down samples were subjected to western blot using anti-Rac1 antibody and the level of GTP-bound Rac1 was quantified by densitometry, normalized against the total amount of Rac1 in the cell lysates. Data represent means ± s.e.m. (error bars), $n = 3$. (left panel) (**d**,**e**) NIH3T3 cells were infected with retroviral combinations of WT GRK6 and two DN forms of ELMO, ELMO1 (T625) and ELMO2 (T615) (**d**), retroviral combinations of WT GRK6 and a DN form of GULP, GULP (PTB), as indicated (**e**). The retrovirus-infected NIH3T3 cells were subjected to the engulfment assay. Percentages of the phagocytes carrying the engulfed thymocytes were determined by FACS. All the phagocytosis experiments were done at least three times, and the average numbers are shown with s.e.m. n.s., not significant. $^{***}P < 0.001$.

Thus, we examined if the GRK6-mediated engulfment pathway was related to these two signalling pathways. We generated DN ELMO mutants, ELMO1 and ELMO2, by truncating their C-terminal regions[23] and a DN GULP mutant by eliminating the phosphotyrosine-binding domain of GULP[24] and co-transfected these with GRK6. The expressions of both the ELMO mutants (Fig. 2d) and the GULP mutant (Fig. 2e) did not affect GRK6-mediated enhancement of apoptotic cell engulfment. These results suggested that the GRK6-mediated engulfment pathway was largely independent of two known pathways.

GIT1 enhances GRK6-mediated engulfment. To search for molecules that could be involved in GRK6-mediated Rac1 activation, we focused on the GRK-interacting ADP ribosylation factor GTPase-activating protein1 (GIT1). GIT1 is one of the few non-receptor proteins that interact with GRK6[25]. However, a functional relationship between GRK6 and GIT1 and the binding region of GIT1 required for this interaction have not been established. GIT1 is expressed in various types of tissues and cells[16]. We confirmed that GIT1 was expressed in NIH3T3 cells, BMDMs and splenic macrophages (Supplementary Fig. S5a). Furthermore, GRK6 deficiency did not affect GIT1 expression in BMDMs (Supplementary Fig. S5b). GIT1 expression alone slightly increased the engulfment of apoptotic cells by NIH3T3 cells (Fig. 3a). However, when GIT1 was co-expressed with GRK6, GIT1 enhanced GRK6-mediated engulfment (Fig. 3a). To identify the amino-acid residues or region of GIT1 that were responsible for GRK6-mediated engulfment, we made some point[26] and deletion[27] mutants of GIT1, as shown in Fig. 3b and Supplementary Fig. S6a. GIT1 (R39K) expression, which lacks the ADP ribosylation factor–GTPase-activator protein activity, had no effect on the GRK6-mediated engulfment (Supplementary Fig. S6b). In comparison, mutants that lacked the coiled-coil domain of GIT1, GIT1(ΔC) and GIT1(ΔAC) significantly attenuated the GRK6-mediated engulfment (Fig. 3a). These GIT1 mutants also inhibited the Rac1 activation by GRK6 (Fig. 3c). Immunoprecipitation experiments revealed that GRK6 interacted with GIT1 (Fig. 3d,e) independently of its kinase activity (Fig. 3f), although GRK6 directly phosphorylated GIT1 (Supplementary Fig. S7). Because the coiled-coil domain-deleted GIT1 mutants did not immunoprecipitate with GRK6, the coiled-coil domain was important for its interaction with GRK6 (Fig. 3d). This GRK6/GIT1 complex did not affect the GIT1-regulated signalling pathways that were previously reported[20] (Supplementary Fig. S8).

Radixin and moesin contribute to GRK6-mediated signalling. To further characterize the GRK6-mediated pathway for apoptotic engulfment, we employed a newly developed phosphoproteomic approach to identify target proteins for GRK6[28]. We prepared three phosphoprotein-enriched fractions from vector-infected, GRK6 (WT)-infected and GRK6 (K215R)-infected NIH3T3 cells. The lysate proteins were labelled with one of the three different fluorescent probes: Vector: Cy2 (shown as blue pseudocolor), GRK6: Cy3 (shown as red pseudocolor) and

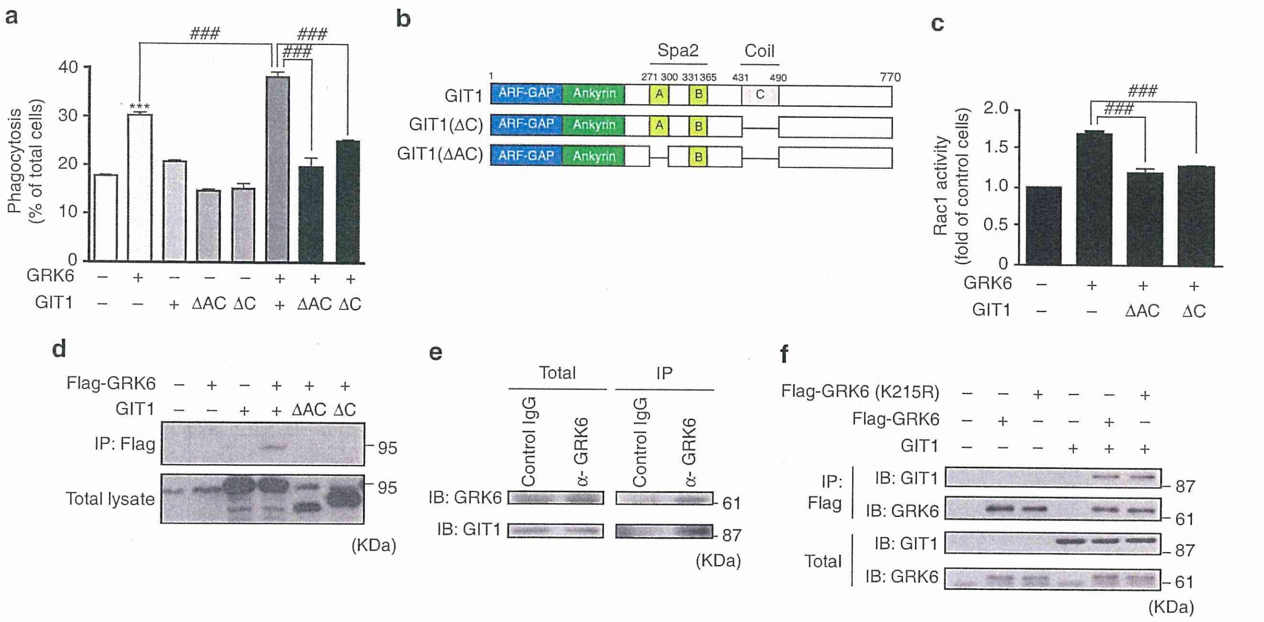

Figure 3 | GIT1 is involved in GRK6-mediated apoptotic engulfment. (**a**) NIH3T3 cells (4×10^4 cells) infected with the indicated retroviruses were co-cultured at 37 °C for 90 min with 1×10^6 cells CMFDA-labelled WT thymocytes. Percentages of the phagocytes carrying the engulfed thymocytes were determined by FACS. The experiments were done at least three times, and the average numbers are shown with s.e.m. (**b**) Schematic representation of GIT1 and its deletion mutants, GIT1 (ΔC) and GIT1 (ΔAC), used in this study. The numbers indicate the positions of the amino acids. (**c**) The activation state of Rac1 in NIH3T3 cells infected with the indicated retroviruses was measured in GTP-Rac1 pull-down assays with GST-CRIB. Data represent means ± s.e.m. (error bars) of four independent experiments. (**d**) HEK293 cell lysates transiently transfected with the indicated plasmids were immunoprecipitated with anti-Flag antibody. Western blot was performed with anti-GIT1 antibody. (**e**) Cell extracts of BMDM from WT mice were immunoprecipitated with normal rabbit IgG or anti-GRK6 antibody. The total lysates and immunoprecipitates (IPs) of BMDMs were immunoblotted (IB) with anti-GRK6 and anti-GIT1 antibodies. (**f**) NIH3T3 cell lysates infected with the indicated retroviruses were immunoprecipitated with anti-Flag antibody. The IPs were subjected to western blot analysis with anti-GRK6 and anti-GIT1 antibodies. All the immunoprecipitation experiments were done at least three times, and representative data are shown. $^{***}P<0.001$, $^{\#\#\#}P<0.001$.

GRK6 (K215R): Cy5 (shown as green pseudocolor). The labelled proteins in each lysate were mixed together, and the mixture was subjected to two-dimensional difference gel electrophoresis (2D-DIGE) followed by fluorescence scanning (Fig. 4a). A small proportion of spots showed a GRK6-induced increase in their acidic forms. We picked out several of these red spots and analysed their protein sequences by mass spectrometry (MS) combined with liquid chromatography. This showed that these proteins were radixin and moesin (Fig. 4b), both of which belong to the same protein ezrin/radixin/mosein (ERM) family. These proteins are known to link integral membrane proteins to the cortical actin cytoskeleton located beneath the plasma membrane, thereby contributing to cytoskeletal remodelling[17] and engulfment[29]. Phosphorylation at a carboxy-terminal threonine residue (Thr567 of ezrin, Thr564 of radixin and Thr558 of moesin) has been implicated in the function of ERM family proteins[30,31]. Therefore, we first examined whether phosphorylation at these sites was induced by the GRK6 overexpression in NIH3T3 cells. Western blotting using an anti-phosphorylated ERM antibody showed that radixin and moesin phosphorylation was increased in NIH3T3 cells due to GRK6 expression (Fig. 4c). This specific phosphorylation was also examined by 2D-western blotting. In this detection system, chemiluminescent signals from the anti-ERM antibody or the phospho-ERM antibody were simultaneously detected with the fluorescent probes used for protein labelling of the lysate mixtures of NIH3T3 cells that expressed WT GRK6 (labelled with Cy3) and GRK6 (K215R) (labelled with Cy5) (Supplementary Fig. S9). Accordingly, we could confirm that these spots had shifted to the more acidic side of the membrane due to GRK6 overexpression and corresponded to phosphorylated ERMs.

We next compared the amounts of the phosphorylated forms of ERMs in BMDMs prepared from WT and GRK6-deficient mice. This revealed that phosphorylated moesin, which is the most abundant and main ERM protein in BMDMs, was significantly decreased in GRK6-deficient BMDMs, which indicated that GRK6 was involved in moesin phosphorylation at its carboxy terminus *in vivo* (Fig. 4d). However, GRK6 did not directly phosphorylate radixin and moesin (Supplementary Fig. S10). ERM phosphorylation by GRK6 was significantly attenuated by the expression of GIT1 mutants that lacked the coiled-coil domain, which suggested that ERM phosphorylation was dependent on the GRK6/GIT1 complex (Fig. 4e). In comparison, GRK6-induced ERM phosphorylation was not affected by Y27632, U0126 and LY294002 (Supplementary Fig. S11), which suggested that Rho-kinase, MEK/ERK and phosphatidylinositol-3-kinase were not involved in ERM phosphorylation. When siRNAs for radixin or moesin were transfected into GRK6-overexpressing NIH3T3 cells, engulfment by these cells was markedly attenuated without affecting the GRK6 expression level (Fig. 4f, Supplementary Fig. S12). These results suggest that radixin and moesin phosphorylation contributes to the GRK6-mediated signalling pathway.

GRK6-deficient mice exhibit an autoimmune-like disease. An *in vivo* defect in apoptotic cell removal reportedly caused the development of an autoimmune disease that resembled human SLE[32]. Thus, we examined whether GRK6-deficient mice

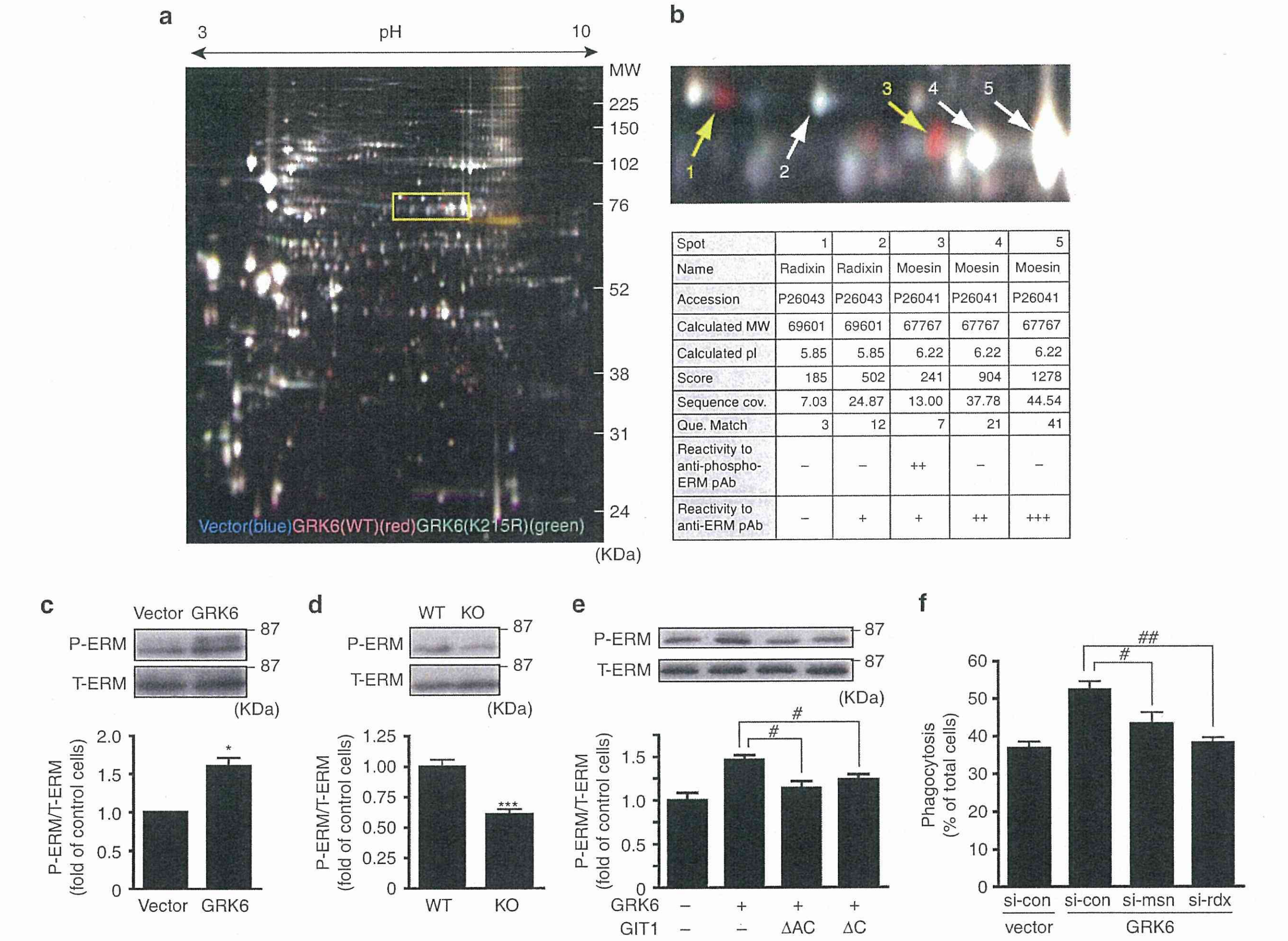

Spot	1	2	3	4	5
Name	Radixin	Radixin	Moesin	Moesin	Moesin
Accession	P26043	P26043	P26041	P26041	P26041
Calculated MW	69601	69601	67767	67767	67767
Calculated pI	5.85	5.85	6.22	6.22	6.22
Score	185	502	241	904	1278
Sequence cov.	7.03	24.87	13.00	37.78	44.54
Que. Match	3	12	7	21	41
Reactivity to anti-phospho-ERM pAb	–	–	++	–	–
Reactivity to anti-ERM pAb	–	+	+	++	+++

Figure 4 | Radixin and moesin phosphorylation is induced by GRK6. (**a**) A representative gel image of 2D-DIGE of phosphoprotein fractions from NIH3T3 cells infected with the empty retrovirus vector (Cy2-labelled, blue), the virus carrying the cDNA for WT GRK6 (Cy3-labelled, red) or GRK6 (K215R) (Cy5-labelled, green). (**b**) Zoom-in view of an area in **a** representing GRK6 (WT)-induced (yellow arrow, red spot) and unchanged (white arrow, white spot) protein spots. The table summarizes the protein identity, accession number, calculated molecular weight, calculated pI, Mascot score, sequence coverage, query match and reactivity to anti-phospho-ERM antibody that specifically recognizes Thr567 of ezrin, Thr564 of radixin and Thr558 of moesin and anti-ERM antibody for the numbered spots. (**c**) NIH3T3 cells are retrovirally transfected with GRK6. The cell lysates were subjected to immunoblotting with the anti-phospho-ERM antibody or anti-ERM antibody. Data represent means ± s.e.m. (error bars). (**d**) The cell lysates prepared from BMDMs of WT and GRK6-deficient mice were immunoblotted with the indicated antibodies. Data represent means ± s.e.m. (error bars). (**e**) Cell lysates of NIH3T3 cells infected with the indicated retroviruses were subjected to western blot analysis using anti-phospho-ERM antibody or anti-ERM antibody. (**f**) GRK6 was transfected with siRNA for control, radixin (rdx) or moesin (msn) and subjected to the engulfment assay. All the experiments were done at least three times, and representative data are shown. $^{*}P<0.05$, $^{***}P<0.001$, $^{\#}P<0.05$ and $^{\#\#}P<0.01$. KO, knockout; MW, molecular weight; P-ERM, phospho-ERM; T-ERM, total-ERM.

developed autoimmunity. An increase in the amount of anti-dsDNA in serum is one of the most important and reliable criteria for SLE. We first evaluated levels of anti-dsDNA in sera collected from 40-week-old GRK6-deficient and WT mice. Increased anti-dsDNA antibody levels were detected in GRK6-deficient mice (Fig. 5a). A major pathogenic consequence of autoantibody production is the deposition of immune complexes in the kidney, which leads to glomerulonephritis. Immunohistochemical analysis of kidney sections showed that there was significantly increased IgG deposition in aged GRK6-deficient mice (Fig. 5b). Consistent with IgG deposition, mesangial expansion, which reflects glomerulonephritis, was also observed in the kidneys of GRK6-deficient mice (Fig. 5c). In addition, GRK6-deficient mice developed age-dependent splenomegaly that was associated with increased numbers of splenocytes (Fig. 5d,e). At 40 weeks of age, their spleens were approximately 1.6-fold heavier than WT mouse spleens. The white pulp in the spleen was enlarged in GRK6-deficient mice (Supplementary Fig. S13), as was observed in MFG-E8-deficient mice that developed lupus-like autoimmune disease due to the impaired uptake of apoptotic cells[33]. We also examined changes in the lymphoid and myeloid cell populations in the spleens of 40-week-old GRK6-deficient mice. The ratios of B cells to T cells and the frequencies of $CD11c^{+}$, $CD11b^{+}$ cells and regulatory T cells were similar in WT and GRK6-deficient mice (Supplementary Fig. S14a–c). Double staining with anti-CD19 and anti-CD69 antibodies was also similar in GRK6-deficient and WT mice, which indicated that the splenomegaly in GRK6-deficient mice was not due to aberrant B-cell activation (Supplementary Fig. S14d). However, the ratio of CD4/CD8 T cells increased in GRK6-deficient mice with a decrease in the CD8 T-cell population, similar to MFG-E8-deficient mice[34] (Supplementary Fig. S15a). Therefore,

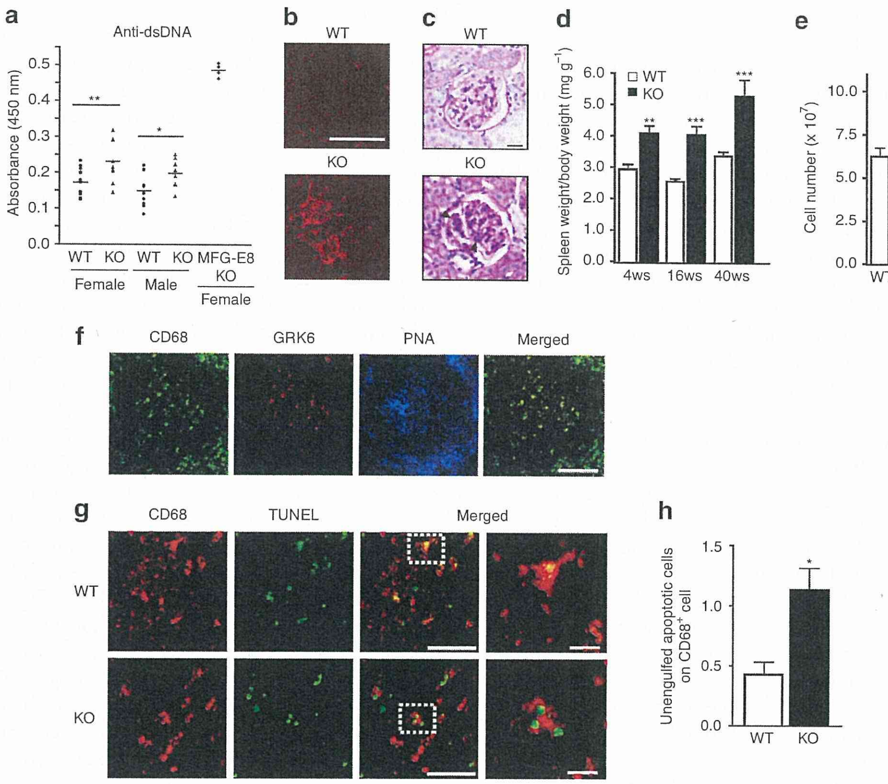

Figure 5 | GRK6-deficient mice spontaneously develop autoimmune disease. (**a**) Serum from 40-week-old control WT and GRK6-deficient female (WT: $n=14$, GRK6-deficient: $n=9$) and male mice (WT: $n=12$, GRK6-deficient: $n=8$) were collected and tested for presence of anti-dsDNA antibodies. Serum from 40-week-old MFG-E8-deficient female mice ($n=4$) was used as a positive control. (**b**) Increased deposition of immune complexes in glomeruli of GRK6-deficient mice at 40 weeks of age was assessed by anti-immunoglobulin staining. Scale bar, 100 μm. (**c**) Paraffin-embedded kidney sections of WT and GRK6-deficient mice at 40 weeks of age were stained using periodic acid-Schiff. Arrowheads indicate a mesangial expansion with increase in matrix and cellularity owing to increased mononuclear cells. Scale bar, 20 μm. (**d**) Spleens isolated from WT and GRK6-deficient mice of 4-week-old ($n=8$), 16-week-old ($n=4$) and 40-week-old ($n=9$) were weighed, and spleen weight relative to body weight were measured. And the average numbers are shown with s.d. (**e**) Splenocytes from WT ($n=7$) and GRK6-deficient mice ($n=6$) of 40-week-old mice were counted, and the numbers were shown in the graph. (**f**) Spleen sections from WT mice were stained with anti-CD68 (green), anti-GRK6 (red) and PNA (blue). The fourth column represents the two-colour (anti-CD68 and anti-GRK6) overlay image. Scale bar, 100 μm. (**g**) Spleen sections from 40-week-old WT and GRK6-deficient mice were double-stained with TUNEL (green) and anti-CD68 antibody (red). Staining profiles were merged in the third column. Scale bar, 50 μm. Enlarged images are shown in the fourth column. Scale bar, 10 μm. (**h**) The numbers of unengulfed cells associated with CD68-positive macrophages were counted for 40-80 macrophages and are presented as the number per macrophages. The average numbers are shown with s.e.m. All immunohistochemical data are representative of four independent experiments. $^{*}P<0.05$, $^{**}P<0.01$ and $^{***}P<0.001$. KO, knockout.

these results support the hypothesis that GRK6-deficient mice developed an autoimmune phenotype, though the symptoms were mild. We also found differences in the $CD8^+$ T-cell populations that mainly affect lupus[34] (Supplementary Fig. S15b). Naive T cells ($CD44^{lo}$ and $CD62L^{hi}$) were decreased in GRK6-deficient mice, whereas memory T cells ($CD44^{hi}$) were increased in these mice. $CD8^+$ memory T-cell populations characterized by CD44 expression can be subdivided into effector (low levels of CD62L) and central memory T cells (high levels of CD62L)[35]. In GRK6-deficient mice, the ratio of $CD62L^{lo}/CD62L^{hi}$ cells among the $CD8^+$ memory T-cell population was increased, which indicated that effector memory T cells had increased reminiscent of aged MFG-E8-deficient mice[34] (Supplementary Fig. S15b). These results suggested that $CD8^+$ T-cell activation was induced by the increased presentation of apoptotic cell-associated antigens by splenic antigen-presenting cells. In young GRK6-deficient mice at 8 weeks of age, no significant abnormalities were found in their spleen cell subsets (Supplementary Fig. S16).

GRK6 is involved in apoptotic cell clearance by macrophages. Macrophages in the germinal centre of the spleen are involved in removing apoptotic B cells. Inefficient engulfment by macrophages supposedly triggers immune responses, which results in SLE-like autoimmunity in mice[33,36,37]. Because we had detected autoimmune properties and abnormalities of the spleen in GRK6-deficient mice, we examined whether GRK6 was expressed by germinal centre macrophages, which were characterized by their CD68 expression. Immunohistochemical staining revealed that GRK6 was expressed in $CD68^+$ macrophages in the germinal centre (Fig. 5f). TdT-mediated dUTP nick end labeling (TUNEL)-stained apoptotic cells were also observed in this area (Fig. 5g). Furthermore, more TUNEL-positive cells were associated with $CD68^+$ macrophages in GRK6-deficient mice, which indicated that many undigested apoptotic cells were present in the spleens of GRK6-deficient mice (Fig. 5h). The numbers of $CD68^+$ macrophages in the white spleen pulp of GRK6-deficient mice were the same as in WT mice, indicating that GRK6 did not affect the development of these macrophages (Supplementary Fig. S17). GRK6 was not involved in the cells' growth, differentiation or apoptosis (Supplementary Fig. S18). Therefore, GRK6 has an important role in the removal of apoptotic B cells by macrophages in the germinal centre without affecting the development, cell growth, differentiation or apoptosis of these macrophages.

We next examined whether the GRK6 expression level was linked to autoimmune diseases. The MRL/*lpr* mouse is a well-known mouse model of SLE. Immunohistochemical analysis of the spleens from MRL/*lpr* mice revealed that the GRK6 expression levels in many splenic macrophages of these mice were markedly increased (Supplementary Fig. S19a,b), which was accompanied with an increase in the numbers of macrophages (Supplementary Fig. S19c). Then, we examined whether GRK6 expression was altered in the macrophages of SLE patients. Among 1,528 autopsies, we could find 6 cases diagnosed with SLE, which is a relatively rare disease. Among these samples, we found an autopsied spleen that had a high expression level of GRK6 in inflammatory cells compared with that of non-SLE patients (Supplementary Fig. S19d).

GRK6 regulates engulfment of senescent red blood cells. Immunohistochemical analysis showed that GRK6 was expressed not only in CD68$^+$ macrophages in the white pulp but also in red pulp macrophages, which was characterized by their expressions of F4/80$^+$ (Fig. 6a). Red pulp macrophages have a role in removing senescent red blood cells, thereby contributing to iron recycling in the body. Dead red blood cells express phosphatidylserine, and their clearance is mediated by phosphatidylserine recognition[38,39]. Thus, we examined the involvement of GRK6 in the removal of senescent red blood cells, a defect of which leads to iron deposition in the red pulp[40]. Splenic red macrophages isolated from GRK6-deficient mice exhibited a defect in their ability to take up dead red blood cells *in vitro* (Fig. 6b). We also examined the phagocytosis of red blood cells by splenic red pulp macrophages *in vivo*. Fluorescently labelled dead red blood cells were injected into WT or GRK6-deficient mice. At 24 h after this injection, splenic macrophages were collected and their engulfment capability was analysed. This showed that the engulfment of dead red blood cells by red pulp macrophages was attenuated in GRK6-deficient mice (Fig. 6c). Perl's Prussian staining, which specifically stains iron, revealed that there was increased iron accumulation in the spleen red pulp of GRK6-deficient mice (Fig. 6d). Quantitative determinations of the iron contents in spleens also showed that splenic iron concentrations were increased in GRK6-deficient mice (Fig. 6e). However, the numbers of red pulp splenic macrophages were not decreased in GRK6-deficient mice (Fig. 6f), which indicated that iron deposition was not due to the abnormal development of splenic red pulp macrophages. Expression levels of ferroportin-1, a major iron exporter and hepcidin, an inhibitor of ferroportin-1, were the same in the spleens and livers of WT and GRK6-deficient mice (Fig. 6g, Supplementary Fig. S20). This suggested that iron export was normal in splenic macrophages of GRK6-deficient mice. In addition, GRK6-deficient mice did not exhibit any abnormal red pulp macrophage populations[41,42] in their spleens (Supplementary Fig. S21). These results suggested that iron deposition in GRK6-deficient mice was caused by inefficient erythrophagocytosis. However, serum iron parameters and the life spans of red blood cells were normal in GRK6-deficient mice (Supplementary Tables 1 and 2 and Supplementary Fig. S22).

We finally compared iron deposition in the spleens of GRK6-deficient mice with that in WT mice after acute anaemia. Acute haemolysis induced by injecting phenylhydrazine is accompanied by shrinkage of the white pulp and causes an enlargement of the red pulp due to an influx of dead red blood cells[43] (Supplementary Fig. S23a). More iron was deposited in the spleens of GRK6-deficient mice after phenylhydrazine injection (Supplementary Fig. S23b). Similar results were obtained after inducing acute anaemia by phlebotomy (Supplementary Fig. S23c).

Discussion

GRK6 is a member of the GRK family of proteins that were initially identified as kinases responsible for the desensitization and downregulation of GPCRs. In this report, we identified GRK6 as an important molecule that promotes efficient apoptotic cell engulfment by several types of macrophages. A deficiency of this molecule resulted in an autoimmune-like disease and splenic iron accumulation in these mice. GRK6-mediated engulfment was largely independent of two well-established intracellular engulfment pathways, DOCK180/ELMO/Rac1 and GULP/Rac1, but did require GIT1 and the phosphorylation of radixin and moesin.

Both GRK2 and GRK6 expressions enhanced apoptotic engulfment. However, the promotion of apoptotic cell engulfment by GRK6 but not GRK2 depends on its kinase activity. A previous report showed that GRK2 positively regulated integrin-dependent epithelial cell migration in a kinase activity-independent manner, which was orchestrated by GIT1[20]. The function of GRK2 in cell migration was regulated by its phosphorylation at certain tyrosine and serine residues[20,44], which led to the interaction of GRK2 with GIT1. This interaction modulates the Rac1/PAK/MEK/ERK1/2 pathway in response to sphingosine-1-phosphate and adhesion[20]. In contrast, the GRK6–GIT1 complex did not significantly influence this pathway (Supplementary Fig. S8). Considering these differences, the pro-migratory or pro-engulfmental signal transduction pathway mediated by GRK2[44,45] or GRK6 is regulated by distinct molecular mechanisms, although GIT1 is common to both the pathways. GRK2 was reported to directly phosphorylate ERM[46], whereas it did not undergo direct phosphorylation by GRK6. This may also contribute to the different signalling pathways by the two GRKs. The molecular mechanism by which GRK2 or GRK6 defines its specific signal transduction pathway will be an interesting theme for future studies.

With regard to the clearance of senescent red blood cells by splenic macrophages, the CD47-SHPS-1 regulatory system has been well studied[47]. The CD47-SHPS-1 system defines self- and non-self recognition by macrophages, which generates the so-called 'Don't eat me signal' that enables viable red blood cells to escape engulfment by phagocytes. In this study, we found that GRK6 promoted the engulfment of senescent red blood cells by red splenic macrophages and contributed to iron homoeostasis. A recent report[40] showed that Spic-deficient mice selectively lost splenic red pulp macrophages. In these mice, iron deposition in their spleens was observed due to the inefficient engulfment of dead red blood cells. In spite of this iron deposition, Spic-deficient mice did not show any significant abnormalities in total iron homoeostasis, which was similar to GRK6-deficient mice. To date, studies on the diseases of iron metabolism have usually focused on the proteins that directly alter iron transport, such as iron transporters/exporters, receptors for iron-binding proteins or the regulators of the activities of these transporters and receptors. Our study provides a new model of human iron disorders in the spleen. GRK6 may be a candidate gene that is responsible for iron overload in some patients.

In summary, we revealed that GRK6 was involved in apoptotic cell clearance by two independent subsets of macrophages in the spleen. GRK6 greatly contributed to removing unnecessary B cells by splenic white pulp macrophages and removing senescent red blood cells by splenic red pulp macrophages. However, we cannot rule out the possibility that some unidentified roles for GRK6, other than engulfment, influence the phenotypes of GRK6-deficient mice, as our experiments were performed using GRK6 systemic knockout mice. Thus, to conclude that the phenotypes observed here were due to engulfment defects by GRK6-deficient macrophages, it will be necessary to examine the phenotypes of GRK6-deficient mice after transplanting bone marrow cells from WT mice and vice versa.

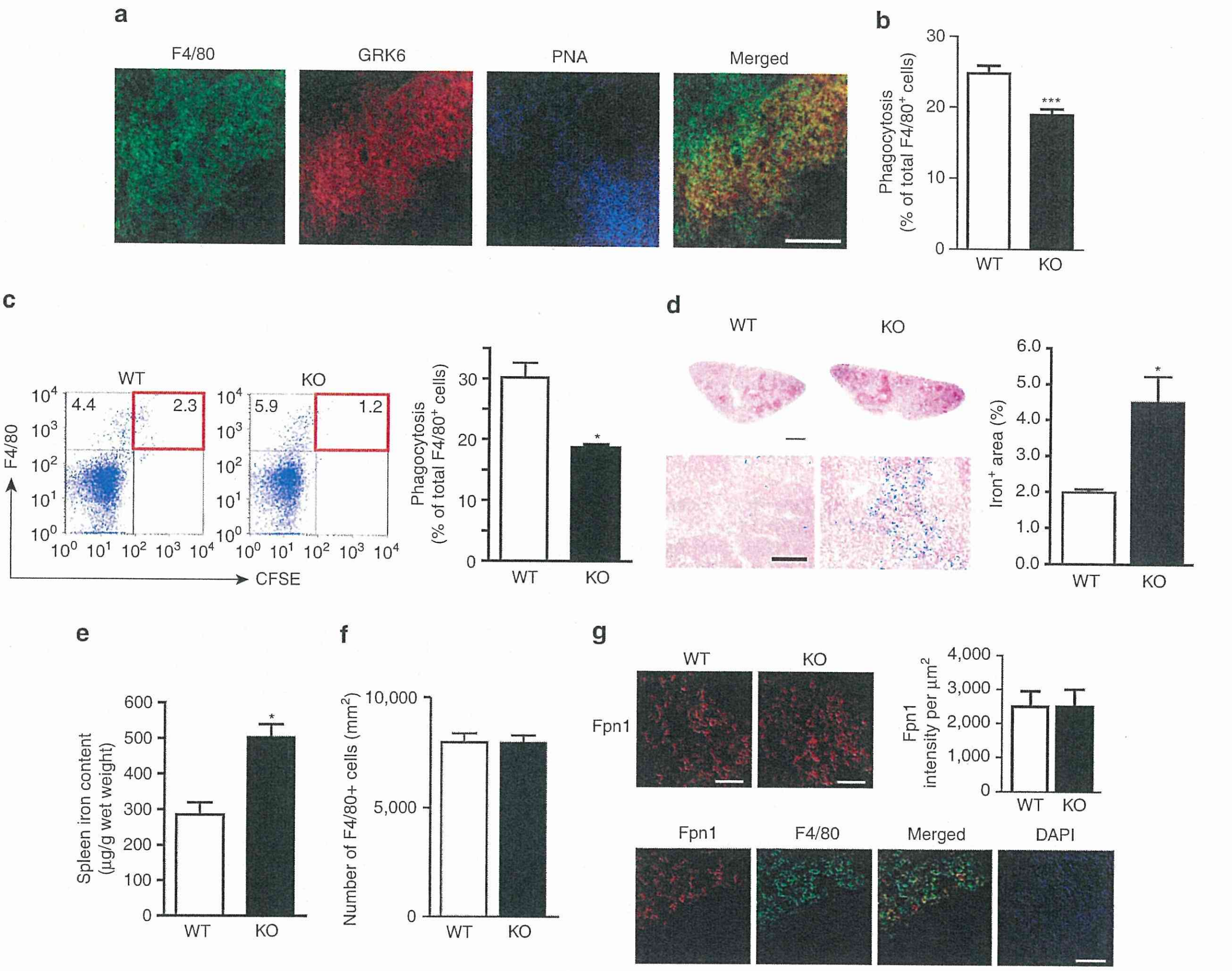

Figure 6 | GRK6-deficient mice manifest iron accumulation in splenic red pulp. (**a**) Spleen sections from WT mice were stained with anti-F4/80 antibody (green), anti-GRK6 antibody (red) and peanut agglutinin (PNA) (blue). The fourth column is the merged image of F4/80 and GRK6. Scale bar, 100 µm. (**b**) Splenic cells from WT and GRK6-deficient mice (1×10^6 per well) were co-cultured with CMFDA-labelled apoptotic red blood cells (4×10^7/well) for 90 min at 37 °C. Percentage of F4/80-positive cells carrying the engulfed red blood cells was determined by FACS analysis and shown in the graph. Error bars represent the mean ± s.e.m. $n = 4$. (**c**) Carboxyfluorescein diacetate succinimidyl ester (CFSE)-labelled apoptotic red blood cells were injected to WT and GRK6-deficient mice from tail vein. Percentage of F4/80$^+$ splenic macrophage carrying the labelled red blood cells was evaluated by FACS. All numbers within FACS profiles correspond to the percentage of cells within each region. Error bars represent the mean ± s.e.m. $n = 3$. (**d**) Spleen sections from 16-week-old WT and GRK6-deficient mice were stained with Perl's Prussian blue to visualize the iron deposits. Scale bar, 300 µm. Enlarged images are shown in the lower column. Scale bar, 100 µm. Areas positive for iron staining were quantified and showed as a percentage of the total surface area of the field. The average numbers are shown with s.d. $n = 3$. (**e**) Iron levels of spleens from 16-week-old WT and GRK6-deficient mice on a standard diet were determined. Error bars represent the mean ± s.e.m. $n = 5$. (**f**) The numbers of F4/80$^+$ macrophages in the splenic red pulp were counted in WT and GRK6-deficient mice. The numbers (cells per mm^2) were determined by four different fields (0.045 mm^2) of spleen sections from WT and GRK6-deficient mice. Error bars represent the mean ± s.e.m. $n = 3$. (**g**) Spleen sections from WT and GRK6-deficient mice were stained with anti-ferroportin-1 (Fpn1) antibody. Fpn1 signal intensity in red pulp areas was determined and showed in the graph. Error bars represent the mean ± s.e.m. Representative images of Fpn1 (red) and F4/80 (green), the merged and 4′,6-diamidino-2-phenylindole (DAPI) images are shown. $n = 4$. Scale bar, 50 µm. $^*P < 0.05$ and $^{***}P < 0.001$. KO, knockout.

Methods

In vitro phagocytosis assay. For uptake assays *in vitro*, we used apoptotic thymocytes or red blood cells as preys. Thymocytes or red blood cells from 4- to 8-week-old C57BL/6 mice were isolated and labelled with 1 µM CMFDA (Life Technologies) by incubating them at 37 °C for 30 min. After the labelling, the thymocytes were allowed to undergo apoptosis by treating thymocytes with 10 µM dexamethasone for 4 h at 37 °C. The labelled red blood cells were suspended in PBS and incubated in the incubator (5% CO_2, 37 °C) for 24 h to induce apoptosis. The labelled apoptotic thymocytes or apoptotic red blood cells were added on the NIH3T3 cells (4×10^4 cells) and BMDM (2×10^5 cells) or splenic macrophages (1×10^6 cells), respectively, in a 24-well plate and co-cultured at 37 °C. The NIH3T3 cells, BMDM and splenic macrophages were vigorously washed by PBS, followed by the treatment with 0.2% trypsin containing 1 mM EDTA. The detached cells were analysed by flow cytometry using a FACS Calibur (BD Biosciences).

GTP-Rac1 pull-down assay. Retrovirus-infected cells were lysed by GTP-Rac1 pull-down assay buffer (50 mM Tris-Cl (pH 7.5), 0.1% Triton X-100, 10% glycerol, 150 mM NaCl, 30 mM $MgCl_2$, 1 mM DTT, 1 mM PMSF, 2 µg ml^{-1} leupeptin and 10 µM pepstatin). The lysates were collected and centrifuged at 15,000 r.p.m. for 10 min at 4 °C to remove cell debris. An amount of 10 µg GST-PAK-Rac1/Cdc42 binding domain and 30 µl Glutathione-Sepharose beads were added to each lysate. The mixtures were incubated at 4 °C for 1 h with gentle rotation. After the incubation, they were subjected to a wash by using the pull-down assay buffer and a brief centrifuge (5,000 r.p.m. for 1 min). The wash was repeated twice and, finally, the beads were boiled in 60 μl SDS sample buffer for 5 min at 95 °C. After the centrifuge, the samples were analysed by western blotting using anti-Rac1 antibody (BD Transduction).

***In vivo* phagocytosis assay**. For splenic macrophage uptake assays, we intravenously injected 8×10^7 CMFDA-labelled apoptotic thymocytes into 10- to 12-week-old WT or GRK6-deficient mice. Two hours after the injection, the mice were killed and their spleens were extirpated. The spleens were smashed between two glass slides, and single-cell splenocyte suspensions were stained with anti-CD11b-APC to identify macrophage population after lysis of red blood cells. Cells were analysed by flow cytometry.

Engulfment of red blood cells *in vivo*. Red blood cells isolated from WT mice were suspended in 30 ml PBS and incubated with 5 μM carboxyfluorescein diacetate succinimidyl ester (Invitrogen) for 10 min at room temperature. After the incubation, the cells were washed three times by PBS and suspended in 2 ml PBS. The cell suspension of 200 μl was injected into WT or GRK6-deficient mice. Twenty-four hours after the injection, spleens of the mice were isolated and minced. The isolated splenocytes were stained with anti-F4/80-APC and analysed by flow cytometry.

Immunoprecipitation. NIH3T3 cells or transfected HEK293 cells expressing Flag-GRK6 and HA-GIT1 were washed and scraped by lysis buffer 1 (50 mM HEPES (pH 7.5), 250 mM NaCl, 2 mM EDTA, 10% glycerol, 0.5% NP40, 1 mM Na_3VO_4 and 1 mM NaF) containing protease inhibitors (Nacalai). The scraped cells were incubated on ice for 30 min and centrifuged at 14,000 r.p.m. for 10 min at 4 °C. The supernatant was collected and rotated gently for 90 min at 4 °C after adding 20 μl anti-Flag antibody beads (Sigma). In the experiment to detect the endogenous interaction between GRK6 and GIT1 in BMDM, the cells were lysed in lysis buffer 2 (50 mM Tris-Cl (pH 7.5), 300 mM NaCl, 0.1% SDS, 1% Triton X-100, 0.5% Sodium deoxycholate, 1 mM Na_3VO_4 and 1 mM NaF) containing protease inhibitors (Nacalai). The lysed cells were incubated on ice for 15 min and centrifuged at 14,000 r.p.m. for 10 min at 4 °C. The collected supernatant was then incubated with anti-GRK6 antibody (Santa Cruz Biotechnology) overnight at 4 °C, followed by the incubation with Protein A-Sepharose beads (GE Healthcare) for 2 h. After the incubation, the beads were washed three times by lysis buffer 1 or 2 of 1,000 μl, and 20 μl SDS sample buffer was added to the beads and they were boiled for 5 min at 95 °C. After centrifugation, the supernatant was collected and subjected to SDS gel electrophoresis and western blotting with antibodies (mouse anti-HA (1:2,000 dilution; Roche), rabbit anti-GIT1 (1:2,000 dilution; Santa Cruz Biotechnology), rabbit anti-GRK6 (1:4,000 dilution; Santa Cruz Biotechnology) and horseradish peroxidase-conjugated anti-mouse IgG (1:5,000 dilution; Santa Cruz Biotechnology) or anti-rabbit IgG (1:5,000 dilution; Santa Cruz Biotechnology).

Two-dimensional difference gel electrophoresis. Phosphoprotein-enriched fractions were subjected to 2D-DIGE essentially as described previously[28]. Briefly, total cell lysates were prepared from NIH3T3 cells overexpressing vector alone, GRK6 or GRK6 (K215R). Then, phosphoproteins in each cell lysate were enriched by using the Phosphoprotein Purification Kit (Qiagen), and interfering nonprotein material was subsequently removed (2-D Clean-Up Kit; GE Healthcare). Thirty microgram of the resultant phosphoprotein-enriched fractions were minimally labelled with 400 pmol Cy2, Cy3 or Cy5 fluorescent dye (CyDye DIGE Fluors, GE Healthcare) for 30 min on ice. After quenching the labelling reaction with 10 nmol lysine, these differentially labelled samples were mixed and subjected to first-dimension isoelectric focusing on immobilized pH gradient strips (24 cm; pH 3–10 non-linear) using an Ettan IPGphor II system. The second-dimensional SDS-PAGE was carried out on 9% acrylamide gel. The Cy2, Cy3 and Cy5 signals were individually acquired with a Typhoon 9400 scanner (GE Healthcare).

Protein identification by MS. After obtaining fluorescent images, the 2D-DIGE gel was silver-stained (Thermo Fisher Scientific/Pierce). Protein spots were excised and digested with trypsin (Promega). The resultant peptides were analysed by a capillary liquid chromatography system (Waters/Micromass, Manchester, UK) connected to a Q-TOF2 mass spectrometer (Waters/Micromass). Raw data were acquired and processed using MassLynx version 4.0. (Waters/Micromass) to generate a peak list file for MS/MS ion search. The peak list files were searched against the NCBI non-redundant protein database restricted to *Mus musculus* using the MS/MS ion search on Mascot search engine (Matrix Science).

Immunohistochemistry. Cryosections (4 μm) of the spleen of WT or GRK6-deficient mice were fixed in cold acetone for 10 min and blocked with PBS containing 3% BSA for 1 h. After the blocking, the slides were incubated with anti-GRK6 (1:50 dilution; Santa Cruz Biotechnology), anti-CD68 (1:200 dilution; Serotec), anti-F4/80 (1:200 dilution; Serotec) and PNA (1:50 dilution; Vectashield) overnight at 4 °C, followed by staining with fluorescent-conjugated secondary antibodies. For staining with an antibody against ferroportin-1, livers and spleens of mice were fixed with 4% paraformaldehyde (PFA) overnight at 4 °C and embedded in FSC22 Frozen Section Media (Leica Microsystems). Tissue sections (6 μm in thickness) were blocked with 3% BSA and reacted with anti-ferroportin-1 (1:200; Alpha Diagnostics) overnight at 4 °C. Then, the sections were incubated with AlexaFluor 594 goat anti-rabbit antibody (Invitrogen). TUNEL assays were performed according to the manufacturer's instructions (ApopTag Fluorescein Direct In Situ Apoptosis Detection Kit; Millipore). For detection of immune complex in the kidney, 40-week-old mouse kidneys were fixed with 4% PFA and embedded in OCT compound (Tissue-Tek). Kidney sections that were 4-μm thick were blocked with PBS containing 3% BSA and stained with Cy3-conjugated F(ab′)2 of goat anti-mouse IgG (Jackson ImmunoResearch Laboratories). Perl's Prussian blue stain or hematoxylin and eosin stain was performed according to the manufacturer's protocol (Sigma) by using paraffin-embedded spleen sections fixed by 4% PFA. Kidney sections fixed with 4% PFA were subjected to periodic acid-Schiff stain according to the standard procedures. All the stained sections were observed under a fluorescence microscope (Keyence BZ-9000) or a confocal microscope (Olympus FV10i or Nikon A1Rsi).

Enzyme-linked immunosorbent assay. The serum from 40-week-old WT, GRK6-deficient and MFG-E8-deficient mice was diluted 25 times in PBS, and 100 μl of the diluted serum was added on the 96-well enzyme-linked immunosorbent assay plates coated with double-stranded DNA (Mesacup DNA-II test; MBL). One hour after the incubation at room temperature, the serum was removed and the plates were incubated with horseradish peroxidase-conjugated goat antibody against anti-mouse Ig (G + M + A) (Cappel) for 1 h. The peroxidase activity was detected by the Peroxidase Detection Kit (Sumitomo), and the absorbance of 450 nm was measured by a microplate reader (Berthold Technologies).

Measurement of iron concentration in spleen. Spleens were weighed and digested in 10% trichloroacetic acid with homogenizer and incubated at 65 °C for 24 h with agitation. The solution was centrifuged at 14,000 r.p.m. for 5 min. The supernatant was collected and neutralized with NaOH to adjust pH >2. The resultant solution was subjected to iron measurement by Mettaloassay LS-MPR Kit (AKJ Global Technology, Japan) based on Nitroso-PSAP method according to the manufacturer's protocol. The absorbance of 750 nm was determined by using a spectrometer.

Statistical analysis. The results are represented as means ± s.e.m. from at least three independent experiments. We employed Student's *t*-test for comparisons for two groups and analysis of variance with the Student–Newman–Keuls test for multiple-group comparison.

References

1. Peter, C., Wesselborg, S., Herrmann, M. & Lauber, K. Dangerous attraction: phagocyte recruitment and danger signals of apoptotic and necrotic cells. *Apoptosis* **15**, 1007–1028 (2010).
2. Maderna, P. & Godson, C. Phagocytosis of apoptotic cells and the resolution of inflammation. *Biochim. Biophys. Acta.* **1639**, 141–151 (2003).
3. Kinchen, J. M. *et al.* Two pathways converge at CED-10 to mediate actin rearrangement and corpse removal in *C. elegans*. *Nature* **434**, 93–99 (2005).
4. Nagata, S., Hanayama, R. & Kawane, K. Autoimmunity and the clearance of dead cells. *Cell* **140**, 619–630 (2010).
5. Mangahas, P. M. & Zhou, Z. Clearance of apoptotic cells in *Caenorhabditis elegans*. *Semin. Cell Dev. Biol.* **16**, 295–306 (2005).
6. Albert, M. L., Kim, J. I. & Birge, R. B. alphavbeta5 integrin recruits the CrkII-Dock180-rac1 complex for phagocytosis of apoptotic cells. *Nat. Cell Biol.* **2**, 899–905 (2000).
7. Reddien, P. W. & Horvitz, H. R. The engulfment process of programmed cell death in *Caenorhabditis elegans*. *Annu. Rev. Cell Dev. Biol.* **20**, 193–221 (2004).
8. Penn, R. B., Pronin, A. N. & Benovic, J. L. Regulation of G protein-coupled receptor kinases. *Trends Cardiovasc. Med.* **10**, 81–89 (2000).
9. Premont, R. T. & Gainetdinov, R. R. Physiological roles of G protein-coupled receptor kinases and arrestins. *Annu. Rev. Physiol.* **69**, 511–534 (2007).
10. Reiter, E. & Lefkowitz, R. J. GRKs and beta-arrestins: roles in receptor silencing, trafficking and signaling. *Trends Endocrinol. Metab.* **17**, 159–165 (2006).
11. Moore, C. A., Milano, S. K. & Benovic, J. L. Regulation of receptor trafficking by GRKs and arrestins. *Annu. Rev. Physiol.* **69**, 451–482 (2007).
12. Penela, P., Murga, C., Ribas, C., Lafarga, V. & Mayor, Jr F. The complex G protein-coupled receptor kinase 2 (GRK2) interactome unveils new physiopathological targets. *Br. J. Pharmacol.* **160**, 821–832 (2010).
13. Gurevich, E. V., Tesmer, J. J., Mushegian, A. & Gurevich, V. V. G protein-coupled receptor kinases: more than just kinases and not only for GPCRs. *Pharmacol. Ther.* **133**, 40–69 (2012).
14. Usui, I. *et al.* G protein-coupled receptor kinase 2 mediates endothelin-1-induced insulin resistance via the inhibition of both Galphaq/11 and insulin receptor substrate-1 pathways in 3T3-L1 adipocytes. *Mol. Endocrinol.* **19**, 2760–2768 (2005).

15. Martini, J. S. *et al.* Uncovering G protein-coupled receptor kinase-5 as a histone deacetylase kinase in the nucleus of cardiomyocytes. *Proc. Natl Acad. Sci. USA* **105,** 12457–12462 (2008).
16. Hoefen, R. J. & Berk, B. C. The multifunctional GIT family of proteins. *J. Cell Sci.* **119,** 1469–1475 (2006).
17. Fehon, R. G., McClatchey, A. I. & Bretscher, A. Organizing the cell cortex: the role of ERM proteins. *Nat. Rev. Mol. Cell Biol.* **11,** 276–287 (2010).
18. Gainetdinov, R. R., Premont, R. T., Caron, M. G. & Lefkowitz, R. J. Reply: receptor specificity of G-protein-coupled receptor kinases. *Trends Pharmacol. Sci.* **21,** 366–367 (2000).
19. Simon, V., Robin, M. T., Legrand, C. & Cohen-Tannoudji, J. Endogenous G protein-coupled receptor kinase 6 triggers homologous beta-adrenergic receptor desensitization in primary uterine smooth muscle cells. *Endocrinology* **144,** 3058–3066 (2003).
20. Penela, P. *et al.* G protein-coupled receptor kinase 2 positively regulates epithelial cell migration. *EMBO J.* **27,** 1206–1218 (2008).
21. Nakaya, M., Tanaka, M., Okabe, Y., Hanayama, R. & Nagata, S. Opposite effects of rho family GTPases on engulfment of apoptotic cells by macrophages. *J. Biol. Chem.* **281,** 8836–8842 (2006).
22. Hall, A. G proteins and small GTPases: distant relatives keep in touch. *Science* **280,** 2074–2075 (1998).
23. Brugnera, E. *et al.* Unconventional Rac-GEF activity is mediated through the Dock180-ELMO complex. *Nat. Cell Biol.* **4,** 574–582 (2002).
24. Park, S. Y. *et al.* Requirement of adaptor protein GULP during stabilin-2-mediated cell corpse engulfment. *J. Biol. Chem.* **283,** 10593–10600 (2008).
25. Premont, R. T. *et al.* Beta2-adrenergic receptor regulation by GIT1, a G protein-coupled receptor kinase-associated ADP ribosylation factor GTPase-activating protein. *Proc. Natl Acad. Sci. USA* **95,** 14082–14087 (1998).
26. Mandiyan, V., Andreev, J., Schlessinger, J. & Hubbard, S. R. Crystal structure of the ARF-GAP domain and ankyrin repeats of PYK2-associated protein beta. *EMBO J.* **18,** 6890–6898 (1999).
27. Premont, R. T. *et al.* The GIT/PIX complex: an oligomeric assembly of GIT family ARF GTPase-activating proteins and PIX family Rac1/Cdc42 guanine nucleotide exchange factors. *Cell Signal* **16,** 1001–1011 (2004).
28. Kosako, H. *et al.* Phosphoproteomics reveals new ERK MAP kinase targets and links ERK to nucleoporin-mediated nuclear transport. *Nat. Struct. Mol. Biol.* **16,** 1026–1035 (2009).
29. Erwig, L. P. *et al.* Differential regulation of phagosome maturation in macrophages and dendritic cells mediated by Rho GTPases and ezrin-radixin-moesin (ERM) proteins. *Proc. Natl Acad. Sci. USA* **103,** 12825–12830 (2006).
30. Matsui, T. *et al.* Rho-kinase phosphorylates COOH-terminal threonines of ezrin/radixin/moesin (ERM) proteins and regulates their head-to-tail association. *J. Cell Biol.* **140,** 647–657 (1998).
31. Mangeat, P., Roy, C. & Martin, M. ERM proteins in cell adhesion and membrane dynamics. *Trends Cell Biol.* **9,** 187–192 (1999).
32. Elliott, M. R. & Ravichandran, K. S. Clearance of apoptotic cells: implications in health and disease. *J. Cell Biol.* **189,** 1059–1070 (2010).
33. Hanayama, R. *et al.* Autoimmune disease and impaired uptake of apoptotic cells in MFG-E8-deficient mice. *Science* **304,** 1147–1150 (2004).
34. Peng, Y. & Elkon, K. B. Autoimmunity in MFG-E8-deficient mice is associated with altered trafficking and enhanced cross-presentation of apoptotic cell antigens. *J. Clin. Invest.* **121,** 2221–2241 (2011).
35. Sallusto, F., Geginat, J. & Lanzavecchia, A. Central memory and effector memory T cell subsets: function, generation, and maintenance. *Annu. Rev. Immunol.* **22,** 745–763 (2004).
36. Mukundan, L. *et al.* PPAR-delta senses and orchestrates clearance of apoptotic cells to promote tolerance. *Nat. Med.* **15,** 1266–1272 (2009).
37. A-Gonzalez., N. *et al.* Apoptotic cells promote their own clearance and immune tolerance through activation of the nuclear receptor LXR. *Immunity* **31,** 245–258 (2009).
38. McEvoy, L., Williamson, P. & Schlegel, R. A. Membrane phospholipid asymmetry as a determinant of erythrocyte recognition by macrophages. *Proc. Natl Acad. Sci. USA* **83,** 3311–3315 (1986).
39. Connor, J., Pak, C. C. & Schroit, A. J. Exposure of phosphatidylserine in the outer leaflet of human red blood cells. Relationship to cell density, cell age, and clearance by mononuclear cells. *J. Biol. Chem.* **269,** 2399–2404 (1994).
40. Kohyama, M. *et al.* Role for Spi-C in the development of red pulp macrophages and splenic iron homeostasis. *Nature* **457,** 318–321 (2009).
41. Chow, A. *et al.* Bone marrow CD169 + macrophages promote the retention of hematopoietic stem and progenitor cells in the mesenchymal stem cell niche. *J. Exp. Med.* **208,** 261–271 (2011).
42. Hashimoto, D. *et al.* Pretransplant CSF-1 therapy expands recipient macrophages and ameliorates GVHD after allogeneic hematopoietic cell transplantation. *J. Exp. Med.* **208,** 1069–1082 (2011).
43. Tolosano, E. *et al.* Enhanced splenomegaly and severe liver inflammation in haptoglobin/hemopexin double-null mice after acute hemolysis. *Blood* **100,** 4201–4208 (2002).
44. Lafarga, V., Aymerich, I., Tapia, O., Mayor, Jr F. & Penela, P. A novel GRK2/HDAC6 interaction modulates cell spreading and motility. *EMBO J.* **31,** 856–869 (2012).
45. Ribas, C. *et al.* The G protein-coupled receptor kinase (GRK) interactome: role of GRKs in GPCR regulation and signaling. *Biochim. Biophys. Acta.* **1768,** 913–922 (2007).
46. Cant, S. H. & Pitcher, J. A. G protein-coupled receptor kinase 2-mediated phosphorylation of ezrin is required for G protein-coupled receptor-dependent reorganization of the actin cytoskeleton. *Mol. Biol. Cell* **16,** 3088–3099 (2005).
47. Oldenborg, P. A. *et al.* Role of CD47 as a marker of self on red blood cells. *Science* **288,** 2051–2054 (2000).

Acknowledgements

We thank Dr R.T. Premont (Duke University) for GRK6-KO mice. We thank Mr K. Fujita (Tokyo Medical University) for his expert assistance. This study was supported by grants from the Ministry of Education, Culture, Sports, Science, and Technology of Japan (M.Na., M.Ni. and H.Ku.); from Grant-in-Aid for Scientific Research on Innovative Areas (M.Ni.); from Grant-in-Aid for Scientific Research on Priority Areas (H.Ku.); from The Takeda Science Foundation, The Uehara Memorial Foundation and The Mochida Memorial Foundation for Medical and Pharmaceutical Research (M.Na.); from Cooperative Research Grant of the Institute for Enzyme Research, the University of Tokushima (M.Na., H.Ko., H.T., M.M. and H.Ku.); and from the Funding Program for Next Generation World-Leading Researchers (NEXT Program) (M.T.). We appreciate for the technical supports from the Research Support Center, Graduate School of Medical Sciences, Kyushu University.

Author contributions

M.Na. designed research. M.Na., M.T., A.H., M.O. and S.K. prepared DNA constructs and performed phagocytosis assay, immunoblotting and immunoprecipitation. M.Na., M.T., A.H. and M.O. conducted phalloidin staining and Rac1 pull-down assay. M.Na. and A.H. carried out enzyme-linked immunosorbent assay experiments and analysed spleen cell population by flow cytometer. Two-dimensional difference gel electrophoresis and *in vitro* kinase assay were performed by H.Ko. Protein identification by mass spectrometry was done by H.Ko., N.T., H.T. and M.M. M.Na., T.N., M.T., K.W., M.K. and H.N. stained spleen and kidney sections. M.Na. conducted all the other experiments. H.Ko., M.Ni., Y.S., M.T. and K.I. provided key reagents and intellectual inputs. M.Na. and H.Ku. wrote the paper.

Additional information

Supplementary Information accompanies this paper at http://www.nature.com/naturecommunications

Competing financial interests: The authors declare no competing financial interests.

Reprints and permission information is available online at http://npg.nature.com/reprintsandpermissions/

How to cite this article: Nakaya, M. *et al.* GRK6 deficiency in mice causes autoimmune disease due to impaired apoptotic cell clearance. *Nat. Commun.* 4:1532 doi: 10.1038/ncomms2540 (2013).